JGR Solid Earth

Correspondence to:
A. H. Kohli and J. M. Warren,
ahkohli@stanford.edu;
warrenj@udel.edu

Evidence for a Deep Hydrologic Cycle on Oceanic Transform Faults

Arjun H. Kohli[1] [iD] **and Jessica M. Warren[2]** [iD]

[1]Department of Geophysics, Stanford University, Stanford, CA, USA, [2]Department of Geological Sciences, University of Delaware, Newark, DE, USA

Abstract Oceanic transform faults represent abundant yet relatively unexplored components of the hydrologic cycle in the mantle lithosphere. Current models limit fluid circulation to 600 °C, the thermal limit of earthquakes recorded by teleseismic surveys. However, recent ocean-bottom seismic surveys have located earthquakes at depths corresponding to >1000 °C in modeled thermal structure. To constrain the depth extent of brittle deformation and fluid infiltration, we analyzed peridotite mylonites dredged from the Shaka Transform Fault, Southwest Indian Ridge. Samples range from high strain mylonites that preserve ductile microstructures to lower strain mylonites that are fractured and overprinted by hydrothermal alteration. Microstructural analysis of the high strain samples reveals brittle deformation of pyroxene concomitant with ductile deformation of olivine and growth of amphibole. Porphyroclasts preserve healed fractures filled with fluid inclusions, implying repeated episodes of fracture, fluid infiltration, and healing. The association of hydration features with brittle structures points to seawater, rather than melt, as the fluid source. Textural analysis indicates that strain localization was initiated by grain boundary pinning and that olivine grain size was reduced to ~1 μm in the presence of amphibole. Comparing the amphibole stability field to thermometry estimates for the limit of recrystallization suggests that fluid flow extended to ~650–850 °C. Our results indicate that the hydrologic cycle extends past the brittle-ductile transition and promotes strain localization via hydrolytic weakening and hydration reactions. We propose that seawater infiltration on oceanic transform faults is driven by the seismic cycle and represents a first order control on the rheology of the oceanic lithosphere.

Plain Language Summary Fluids strongly impact the behavior of faults in the Earth's lithosphere. Faults often act as pathways for fluid flow, so transform faults that offset mid-ocean ridges may be potential conduits for seawater. To determine whether and how deep seawater circulates within transform faults, we studied rocks dredged from a major transform fault in the southern Atlantic Ocean. We identified water-bearing minerals that form at high temperature through interactions of seawater and mantle rocks, indicating that fluids circulated much deeper in the fault than previously thought. We also found trapped fluids inside large mineral grains, which suggests that fluids entered the fault during brief fracturing events, likely caused by deep earthquakes. Our results agree with recent seismic studies that have located earthquakes on Pacific Ocean transforms within a similar temperature range to that recorded by the hydrous minerals. We argue that earthquakes drive deep circulation of seawater on oceanic transform faults, which strongly impacts their strength and seismic properties.

1. Introduction

Oceanic transform faults (OTFs) are the most abundant type of strike-slip fault on Earth, yet little is known about their mechanical and hydrologic properties. Given that faults in the Earth's crust often act as conduits for circulation of surface water at depth (Barton et al., 1995; Lin et al., 2003; Sibson et al., 1975; Townend & Zoback, 2000), OTFs may represent important components of the hydrologic cycle in the oceanic lithosphere. Due to the lack of easily accessible exposures and limited seafloor sampling, few geologic observations have been made to constrain the depth extent of fluid circulation on OTFs.

Current models limit fluid circulation in the oceanic lithosphere to the maximum depth of seismicity and brittle deformation. Global teleseismic surveys of OTFs have concluded that seismicity is limited to depths corresponding to temperatures <600 °C, based on numerical models of OTF thermal structure (Abercrombie & Ekström, 2001; Chen & Molnar, 1983; Engeln et al., 1986; McKenzie et al., 2005).

However, recent ocean-bottom seismic surveys, in conjunction with revised thermal models, show seismicity extending to depths corresponding to ~600–1100 °C (Kuna et al., 2019; McGuire et al., 2012; Roland et al., 2012; Wolfson-Schwehr et al., 2014). These observations of deep seismicity indicate that the 600 °C isotherm is not the limit of brittle deformation but rather represents the upper extent of a brittle-ductile transition zone. This suggests that fluids, in particular seawater, may infiltrate much deeper into the oceanic lithosphere than previously estimated.

If fluids infiltrate the ductile part of OTFs, evidence of hydration during deformation may be preserved in the mineral assemblages and deformation textures of fault rocks. Deformed rocks from OTFs have been sampled in only a few locations by shipboard dredging (Cannat et al., 1990; Cipriani et al., 2009; Farmer & Dick, 1981) and diving (Cannat & Seyler, 1995; Hekinian et al., 1992). While the full range of oceanic lithosphere lithologies has been recovered, only a few dredges have recovered peridotite mylonites (Farmer & Dick, 1981), which form by fault zone deformation to high strains (White et al., 1980). One of the best preserved suites of mylonites comes from the Shaka Transform Fault, Southwest Indian Ridge, where two dredges recovered large amounts of highly deformed peridotites (Jaroslow et al., 1996; Warren & Hirth, 2006). In previous studies of peridotite mylonites from this and other OTFs, deformation was interpreted to have occurred under dry conditions (Jaroslow et al., 1996; Linckens et al., 2011; Matysiak & Trepmann, 2012; Warren & Hirth, 2006). In the Shaka peridotite mylonites, Jaroslow et al. (1996) identified a hydrous mineral phase, amphibole, which occurs in fractures within orthopyroxene porphyroclasts and in veins that crosscut the deformation fabric. In a follow-up study, Warren and Hirth (2006) determined that amphibole formation was not associated with the fine-grained shear zones within the mylonite and thus concluded that deformation occurred under dry conditions.

In this study, we use improved microanalytical techniques to re-examine the Shaka mylonites for evidence of hydration to evaluate the role of fluids in OTF deformation. We identify hydrous phases and determine their relationship to the mylonite microstructure in order to estimate the conditions of strain localization. We analyze samples ranging in strain and hydrous mineralogy to understand how strain localization impacts fault strength and structure. By considering the mineralogy and deformation textures in the context of the fault thermal structure, we place constraints on the depth extent of fluid infiltration and brittle-ductile deformation.

2. Oceanic Transform Fault Mylonites

2.1. Location

Samples were dredged from the SE wall of the Shaka Transform Fault, which is located at 9°E, 53°S on the ultra-slow spreading Southwest Indian Ridge (Figure 1). The fault slip rate at this location, calculated from the GSRM v1.2 model, is 12.9 mm/year (Kreemer et al., 2003). Two dredges (AII107-60, -61) collected highly deformed peridotites along with minor amounts of basalt and diabase (Figure 1, grey stars), during Cruise 107, Leg 6 of the R.V. Atlantis II in 1980 (Farmer & Dick, 1981). Two mylonites in this study, 60-4 and 61-83, were included in a survey of transform fault mylonites by Jaroslow et al. (1996). Microstructures of 61-83 were also studied in detail by Warren and Hirth (2006). In addition to these samples, we selected two other mylonites, 60-5 and 60-7, for analysis.

The exposure of peridotite mylonites on the seafloor means that mechanisms exist on OTFs by which rocks can be uplifted from the high P-T conditions of ductile deformation. We do not constrain the mechanism at Shaka but acknowledge that a large amount of vertical motion (>10 km) was necessary to expose the Shaka samples, similar to exposures of deformed peridotites at other OTFs (e.g., Cannat et al., 1990; Cipriani et al., 2009; Maia et al., 2016). One possible mechanism for uplift on OTFs is a change in the local ridge spreading direction that leads to transtensional or transpressional motions, adding a dip-slip component to the fault. This is observed at the Romanche and Vema transform faults on the Mid-Atlantic Ridge (Bonatti et al., 1994, 2005). Another example is the St. Paul transform fault on the Mid-Atlantic Ridge (Maia et al., 2016), where transpressional motion resulted in uplift of mylonites from depth within a positive "flower" structure. On the Shaka transform fault, vertical motion along the fault in response to oblique plate motion is also the most likely mechanism for uplift given the obliquity of ridge motion on either side of the fault (Dick et al., 2003).
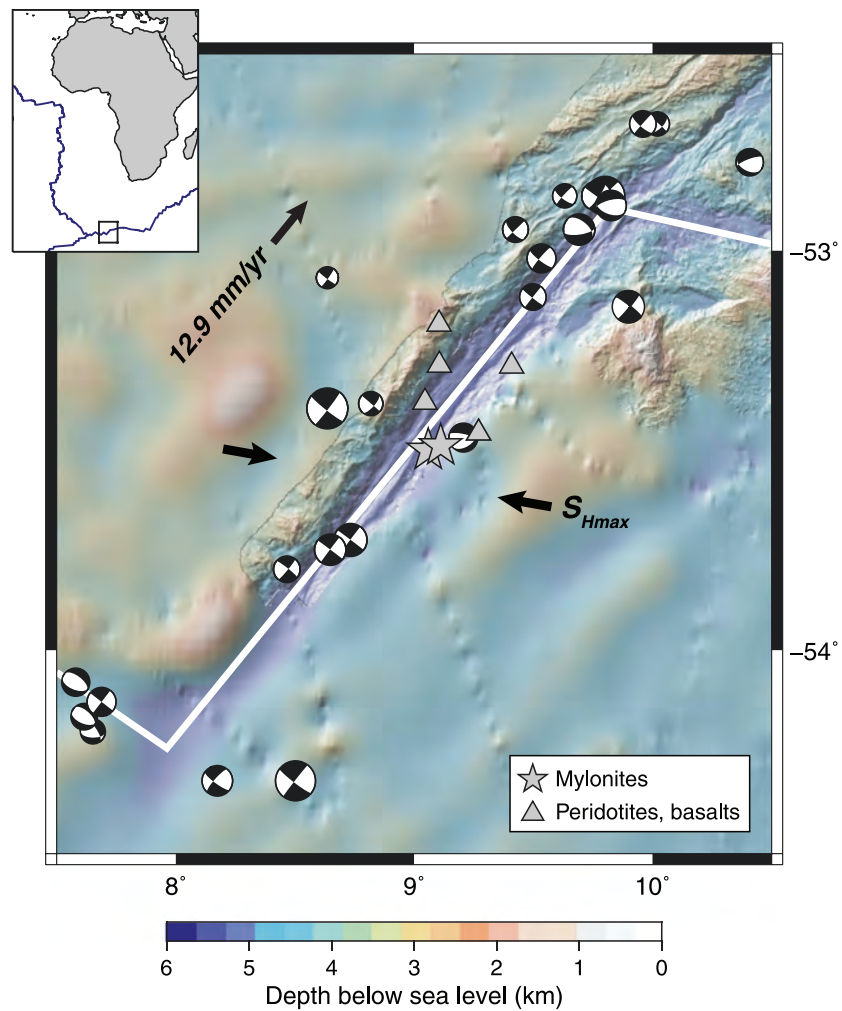
Figure 1. (inset) Location map of the Shaka transform fault on the Southwest Indian Ridge. (main) Bathymetry map created from GeoMapApp (Ryan et al., 2009) using shipboard multibeam data (high resolution) overlain on satellite altimetry data (low resolution). Full spreading rate at this location is 12.9 mm/year (Kreemer et al., 2003). Stars indicate the location of the two dredges (AII-60 and AII-61) that recovered peridotite mylonites. Triangles indicate dredges that recovered undeformed rocks, ranging from basalt to gabbro to peridotite (Farmer & Dick, 1981). Earthquake focal mechanisms sized by magnitude (m_b = 4.5–6.8) are shown from the Global CMT catalog for the period 1950–2019 (Dziewoński et al., 1981; Ekström et al., 2012). S_{Hmax} denotes the direction of the maximum horizontal compressive stress determined by inversion of earthquake focal mechanisms (Heidbach et al., 2018).

2.2. Compositional Analysis

We selected four peridotite mylonites (AII107-60-4, -60-5, -60-7, and -61-83) that are strongly foliated in hand sample. We interpret this foliation to have formed as a result of ductile deformation to high strains in the fault zone. The protolith of the mylonites was peridotite from the oceanic lithosphere, which consists of olivine, orthopyroxene, clinopyroxene, and spinel (e.g., Bodinier et al., 2014; Dick et al., 1984). Analysis of hand samples and thin sections also indicates the presence of additional phases that were deformed along with the peridotite assemblage. Due to the fine-grained nature of these minerals, we used bulk rock analysis by X-ray fluorescence (XRF) and X-ray powder diffraction (XRD) to estimate sample mineralogy. We then used electron backscatter diffraction (EBSD) and energy dispersive spectroscopy (EDS) to further constrain the mineralogy and characterize the deformation microstructures.

2.2.1. Bulk Rock Composition

Bulk rock major element data (Table A1) were collected by XRF at Washington State University GeoAnalytical Lab, following procedures described by Johnson et al. (1999). Loss on ignition, the mass of volatiles lost upon heating the sample powder to ~1000 °C, was used to estimate the hydrous phase
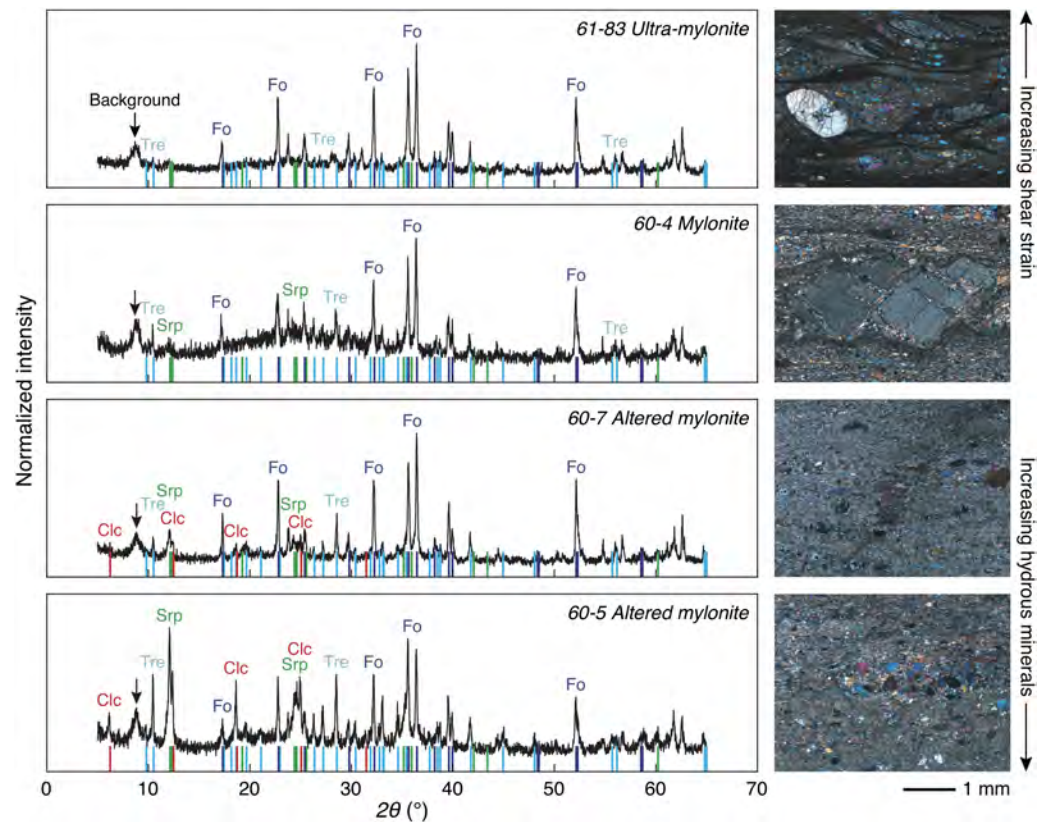
Figure 2. X-ray diffraction spectra and petrographic images (cross-polarized light) of peridotite mylonites. (top to bottom) 61-83, ultra-mylonite; 60-4, mylonite; 60-7, altered mylonite; 60-5, altered mylonite. Major peaks in the spectra are matched by forsterite (Fo) and tremolite (Tre) in all samples. Samples 60-5 and 60-7 have additional peaks that are matched by the three polymorphs of serpentine (Srp) and clinochlore (Clc).

content in each sample. The altered mylonites have higher loss on ignition (4.7, 5.0%) than the higher strain mylonites (2.0, 3.8%), consistent with observations of greater hydrothermal alteration in hand sample and thin section.

2.2.2. XRD

XRD was performed on crushed, millimeter-scale tablets cut from centimeter-scale hand samples. Analyses were conducted by XRD.us using a Shimadzu XRD6000 instrument. We fit spectra using the X'Pert software suite and mineral data from the RRUFF database (Lafuente et al., 2015). Sample mineralogy varies systematically with the degree of deformation (Figure 2). The XRD spectra of the high-strain samples (60-4 and 61-83) are matched by forsterite (Mg-olivine) and tremolite (Ca-amphibole), while the spectra of the altered samples (60-5 and 60-7) also show significant contributions from the three serpentine polymorphs (chrysotile, lizardite, and antigorite) and clinochlore (calcic chlorite). None of the analytical techniques used to determine sample mineralogy allow us to distinguish between the serpentine polymorphs, so we only use the mineral group name hereafter. The strongest signatures of serpentine and chlorite are in altered mylonite 60-5, which also shows the least strain and most hydrothermal alteration in hand sample and thin section. Although these results inform our understanding of the relative compositions of the mylonites, it is clear that the XRD samples do not fully capture the mineralogy. No serpentine is detected in either the ultramylonite or mylonite, although serpentine veins are visible in hand sample and thin section. This suggests that these veins are too sparsely distributed to be adequately sampled by the small amount of powder (1-5 g) used in the XRD measurements.

2.2.3. EBSD-EDS

To map mineral phase relationships and crystallographic orientations, we performed EBSD-EDS analysis on thin sections cut perpendicular to foliation and parallel to lineation (Figure 2). In the following sections, we use directional terminology (vertical and horizontal) with respect to the thin section reference frame.

Because these are dredge samples, we cannot definitively orient the thin sections with respect to the fault zone at depth. However, assuming that the foliation and lineation resulted from strike-slip deformation, we interpret the thin sections to represent a "map view" of the fault, with the lineation (left to right in Figure 2) representing the slip direction and the foliation (in and out of the page in Figure 2) parallel to the vertical fault plane in the Earth.

Data were collected on Oxford Instruments Nordlys-F+ EBSD and X-Max 20-mm^2 EDS detectors on a FEI Quanta 200 scanning electron microscope located in the Department of Plant Biology at the Carnegie Institution at Stanford University. Data were processed using the AZtec 2.0 software package and phase maps, and pole figures were created using the accompanying HKL Channel5 software package. We performed mineral identification, orientation, and composition measurements at step sizes between 0.5 and 5 μm, depending on the smallest grains in the region of interest. Elemental compositions from EDS spectra were used to constrain possible mineral match phases, followed by fitting the EBSD diffraction patterns to quantify mineral abundance and crystallographic orientation.

Using improved detectors and software algorithms, we were able to achieve at least 90% indexed data on the mylonites, compared to ~50–70% in the previous study of ultra-mylonite 61-83 (Warren & Hirth, 2006). The quality of orientation data is assessed using the mean angular deviation, which quantifies the misfit between the calculated orientation based on a crystallographic database and the digitized diffraction pattern. With the AZtec 2.0 system, we were able to use a criterion of mean angular deviation <0.5° for accepting indexed solutions, much stricter than the value of <1° used by Warren and Hirth (2006). We processed the raw EBSD data by (i) removing wild spikes and (ii) extrapolating null solutions based on neighboring orientations. Wild spikes are defined as solutions for which the misorientation angle relative to the average orientation of the eight neighboring points exceeds 10° or the maximum misorientation between any two neighboring points exceeds 10°. After removal of wild spikes, we extrapolated iteratively to fill null solutions based on the most common neighbor orientation at eight, seven, and six neighbors sequentially. The processed maps have ~99% data coverage. Grain boundaries were defined by neighbor-neighbor misorientations ≥10° and pole figures calculated based on 1 point per grain. Grains with <3 data points were excluded from further data analysis as not being sufficiently resolved.

2.2.4. Sample Mineralogy

All samples contain olivine, orthopyroxene, clinopyroxene, and Cr-spinel and are comprised of a fine-grained matrix surrounding porphyroclasts of the coarse-grained protolith. We assume that the protolith of these deformed samples was a lherzolite assemblage with millimeter-scale grain size, similar to the microstructure of typical abyssal peridotites (e.g., Achenbach et al., 2011; Warren et al., 2009). The mylonite foliation is defined by relatively fine-grained (<10 μm) and coarse-grained (>100 μm) layers, which form an anastomosing structure of sub-horizontal shear zones.

We use EBSD-EDS analysis of the fine-grained matrix and select porphyroclasts to further constrain mineralogy. In all samples, tremolite represents a significant fraction of the fine-grained matrix, consistent with the XRD data (Figure 2). In contrast, pyroxene occurs as sparsely distributed porphyroclasts and, in some cases, is largely replaced by tremolite, which may explain why pyroxene was not represented in the XRD data. In the high strain mylonites (61-83 and 60-4), only olivine, orthopyroxene (enstatite), clinopyroxene (diopside), tremolite, and chromite (Cr-spinel) were identified in the EBSD-EDS maps. In the altered mylonites, clinochlore was also identified. We were not able to map the distribution and orientation of serpentine, due to its fine grain size and tendency to polish to lower heights than the other phases. To estimate primary and secondary mineral modes, we performed multiple millimeter-scale, high-resolution maps per sample and integrated the results with the XRD and petrographic observations (Table 1).

3. Microstructural Analysis

While all samples could be termed peridotite "mylonites" due to the degree of grain size reduction, we adopt a further classification to describe the observed variations in deformation and hydrothermal alteration features. Sample 61-83, previously analyzed by Warren and Hirth (2006), is termed "ultra-mylonite" as it shows the most grain size reduction (greatest strain) and the least alteration (Figure 3a). Sample 60-4 is termed "mylonite" as it shows intermediate grain size reduction and limited alteration along grain-scale fractures

Table 1
Sample Classification and Mineralogy

			Mineral modes (wt%)							
ID	Classification	Interpreted location	Olivine	Orthopyroxene	Clinopyroxene	Spinel	Tremolite	Serpentine	Clinochlore	LOI (wt%)
61-83	Ultra-mylonite	Fault core	50	30	<1%	<1%	15	5	0	2.0
60-4	Mylonite	Fault core	45	25	<1%	<1%	20	10	0	3.8
60-7	Altered mylonite	Damage zone	30	10	5	<1%	25	20	10	4.7
60-5	Altered mylonite	Damage zone	25	5	5	<1%	25	25	15	5.0

Note. LOI (loss on ignition) provides an estimate of the wt% volatiles present in each sample. The IGSNs for dredges AII107-6-60 and -61 are WHO000BT4 and WHO000BT5.

(Figure 3b). Samples 60-5 and 60-7 are termed "altered mylonites" as they show the least grain size reduction, relatively weak foliations, and significant areas of alteration within the peridotite matrix and along centimeter- to millimeter-scale fractures (Figures 2c and 2d). Although we cannot reconstruct any spatial relationships between these dredge samples, all samples must have followed the same pressure-temperature path to the surface given their close proximity to each other. The variations in strain and fracture density imply that the ultra-mylonite likely originated closer to the core of the fault zone than the altered mylonites. To place the microstructural and compositional variations of the four samples in the context of fault zone deformation, we characterized the microstructures from the earliest to the latest overprinting features through detailed optical petrography.

3.1. FIPs

The earliest evidence of fluid infiltration in the mylonites is fluid inclusion planes (FIPs) within porphyroclasts and larger recrystallized grains >100 µm diameter (Figure 4). FIPs are found in all major phases (olivine, pyroxene, and spinel) as planar surfaces with approximately spherical fluid inclusions, each ~0.05–
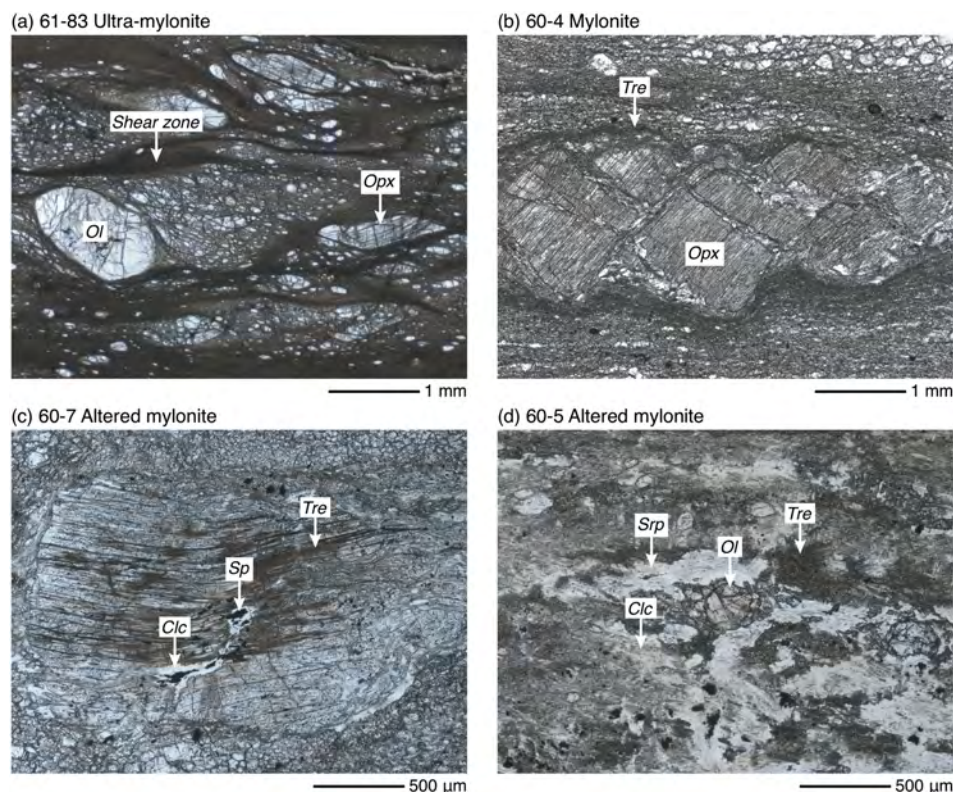
Figure 3. Thin sections of peridotite mylonites cut perpendicular to foliation and parallel to lineation (plane polarized light). Mineral abbreviations: Ol—olivine, Opx—orthopyroxene, Sp—spinel, Tre—tremolite amphibole; Srp—serpentine, and Clc—clinochlore.
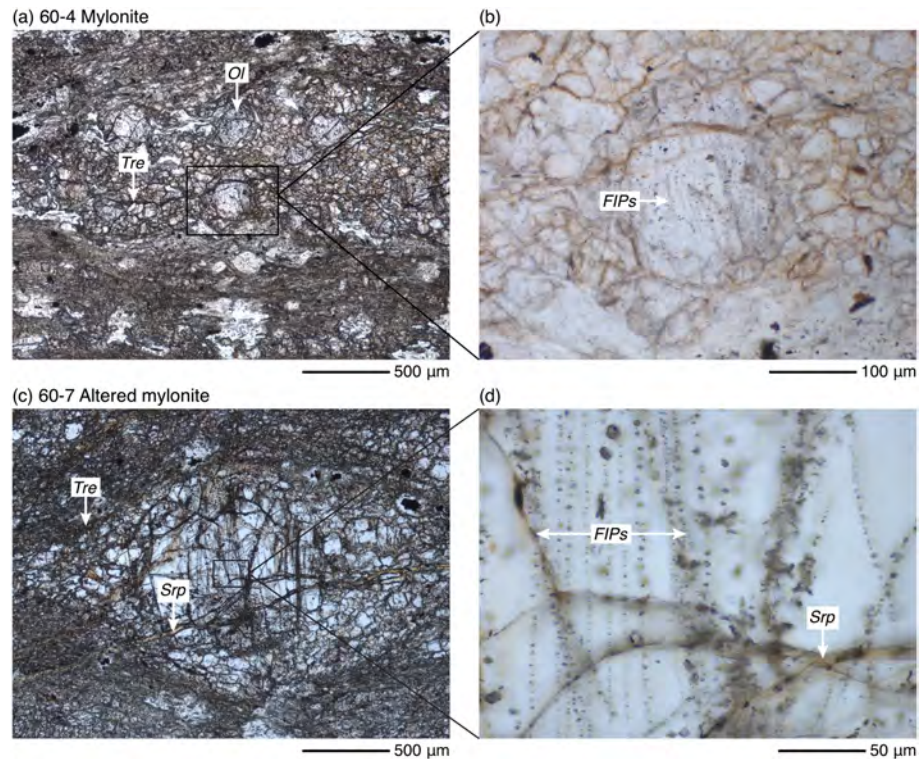
Figure 4. Fluid inclusion microstructures (plane polarized light). (a) Mylonite 60-4 shows alternating coarse- and fine-grained bands in a sub-horizontal, anastomosing fabric. (b) A relatively large recrystallized olivine grain (~100 μm diameter) contains multiple sub-parallel FIPs that are truncated at the grain boundaries. This grain is surrounded by a fine-grained region that contains only sparse, isolated fluid inclusions. (c, d) Altered mylonite 60-7 contains pervasively fractured and partially recrystallized olivine porphyroclasts riddled with sub-vertical FIPs and crosscut by serpentine (Srp) fractures.

5 μm in diameter. Populations of aligned FIPs appear sub-parallel and steeply dipping when viewed through the thin section in 3-D by varying focal depth on an optical microscope. In all samples, FIPs do not occur in recrystallized grains <100 μm diameter and do not crosscut the mylonite fabric, but instead terminate at grain boundaries.

In the mylonite and ultra-mylonite, relic coarse grains often form the core of bands that did not fully recrystallize compared to the rest of the matrix (Figure 4a). Finer grains (~10–100 μm) in these bands are free of microfractures and contain only isolated fluid inclusions (Figure 4b). In contrast, larger grains (>100 μm) show intragranular microfractures and multiple aligned FIPs that terminate at recrystallized grain boundaries (Figure 4c). The two altered mylonites contain large olivine porphyroclasts (1–3 mm) with very similar FIP structures. The porphyroclasts contain more abundant sub-parallel planes and microfractures (Figure 4d), as well as larger individual fluid inclusions (Figure 4e). FIPs in all samples are crosscut by sub-horizontal serpentinized fractures that pervade the surrounding fine-grained matrix.

3.2. High Temperature Hydrothermal Alteration

The next evidence of hydration in the mylonites is the presence of amphibole within grain-scale faults in porphyroclasts. All samples have foliations indicative of macroscopically ductile deformation, but the high strain samples (61-83 and 60-4) also preserve evidence of brittle deformation at the grain-scale. Olivine and orthopyroxene porphyroclasts exhibit intragranular shear zones with offsets up to ~500 μm (Figure 5a). In orthopyroxene, conjugate fault sets are often oriented parallel and perpendicular to clinopyroxene exsolution lamellae (Figures 5a and 5c). These faults appear to incorporate and shear the surrounding peridotite matrix and, in some cases, are associated with healed, sub-vertical fractures (Figure 5a). The matrix fill is composed of fine-grained olivine and tremolite amphibole, with tremolite in some cases presenting as euhedral, bladed crystals ~50–100 μm (Figures 5b and 5d).
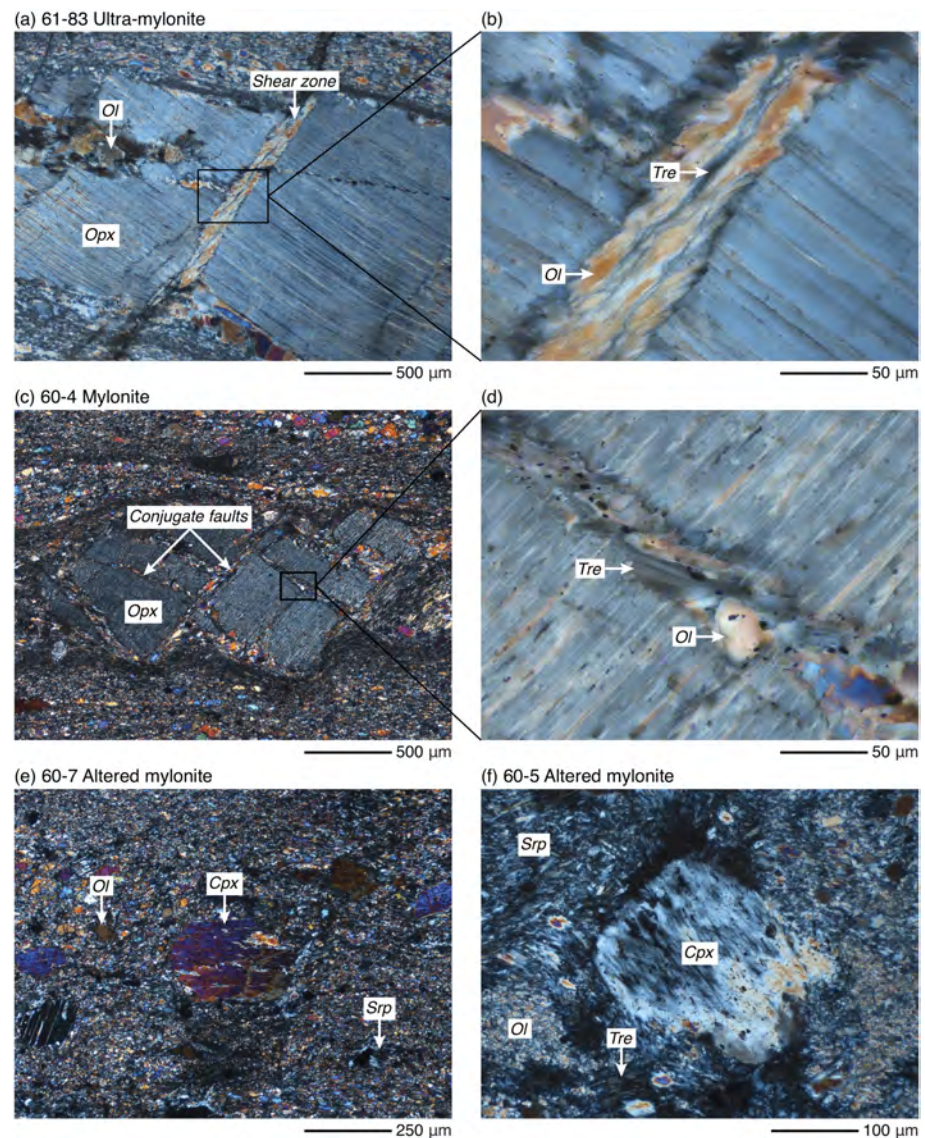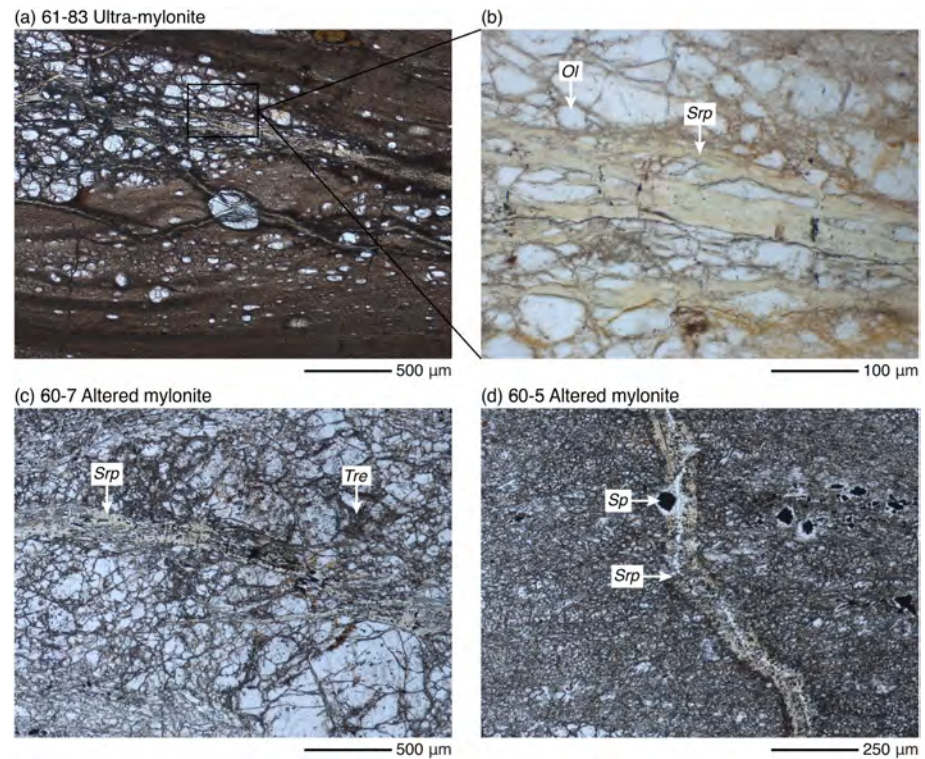
Figure 5. High temperature alteration microstructures (cross-polarized light). (a, b) Ultramylonite 61-83 shows grain-scale faults in orthopyroxene (Opx) porphyroclasts. These intragranular faults appear to incorporate and shear the surrounding matrix of recrystallized olivine (Ol) and tremolite amphibole (Tre). (c, d) Mylonite 60-4 shows conjugate grain-scale faults in orthopyroxene, filled by euhedral to subhedral grains of olivine and tremolite. (e, f) Altered mylonites, 60-7 and 60-5, are relatively depleted in orthopyroxene porphyroclasts but contain clinopyroxene (Cpx) porphyroclasts within a fine-grained matrix of olivine, tremolite, and serpentine (Srp). In (f), the clinopyroxene porphyroclast has been completed altered to tremolite.

The two altered mylonite samples (60-5 and 60-7) do not preserve intragranular faults in porphyroclasts, possibly because they are relatively depleted in orthopyroxene and/or these features have been overprinted by lower temperature hydrothermal alteration (e.g., Figure 3c). Dispersed porphyroclasts of clinopyroxene, up to ~1 mm diameter, are present in relatively low strain regions and do not show any evidence of brittle deformation (Figures 5e and 5f). Tremolite amphibole occurs in the altered mylonites as pseudomorphs after clinopyroxene (Figure 5f) and as fine-grained, massive fill in the olivine-rich regions but is difficult to identify using optical petrography.

3.3. Low Temperature Hydrothermal Alteration

The latest evidence of hydration and brittle deformation is intergranular fracturing of the mylonite matrix and formation of relatively low temperature hydrous phases. Hydrothermal alteration of the original

Figure 6. Low temperature alteration microstructures (plane polarized light). (a, b) Ultramylonite 61-83 contains sub-horizontal serpentine-filled veins concentrated in regions of relatively coarse-grained recrystallized olivine (Ol). (c) Altered mylonite 60-7 contains more abundant serpentine (Srp) veins, which are also concentrated in regions of coarser-grained olivine and relic porphyroclasts. (d) Altered mylonite 60-5 contains sub-vertical fractures filled with serpentine and other hydrous alteration phases. Spinel (Sp) is surrounded by alteration halos of clinochlore.

peridotite matrix to serpentine and clinochlore (calcic chlorite) overprints all other microstructural features (Figure 6). The degree of hydrothermal alteration varies inversely with the degree of grain size reduction, such that the most deformed samples (61-83 and 60-4) have less of an overprint (Figure 3).

Ultra-mylonite 61-83 contains branching, sub-horizontal serpentinized fractures, which appear to preferentially cut regions of relatively coarse-grained recrystallized olivine >100 μm (Figures 6a and 6b). These fractures are relatively thin (up to 50 μm) and sparsely distributed within the fine-grained matrix. Sub-vertical fractures are also present but appear mostly closed and unfilled. Similar features are observed in slightly greater abundance in mylonite 60-4. In contrast, the altered mylonites 60-5 and 60-7 exhibit thicker, more abundant serpentinized fractures (Figures 6c and 6d) and contain wide bands (up to 3 mm) of massive serpentine and chlorite, which completely overprint the peridotite matrix and obscure the high temperature foliation (Figure 3d). In hand sample, the altered mylonites contain both sub-horizontal and sub-vertical fractures that are filled with serpentine.

4. Textural Analysis

Since the deformation microstructures of the altered mylonites are mostly overprinted by low temperature alteration phases (serpentine and chlorite), we focus our analysis on the high strain mylonites (61-83 and 60-4) in order to understand the impact of syn-deformational secondary phases on fault rheology. Warren and Hirth (2006) previously mapped ultramylonite 61-83 and documented sub-horizontal, anastomosing bands of relatively coarse-grained (10–100 μm) and fine-grained (<10 μm) olivine. Olivine exhibited a strong crystallographic preferred orientation (CPO) in the coarse-grained bands, and weak to no CPO in the fine-grained bands. Their EBSD maps also indicated that secondary phases were much more abundant in the fine-grained bands of olivine. Due to limitations of their EBSD system,
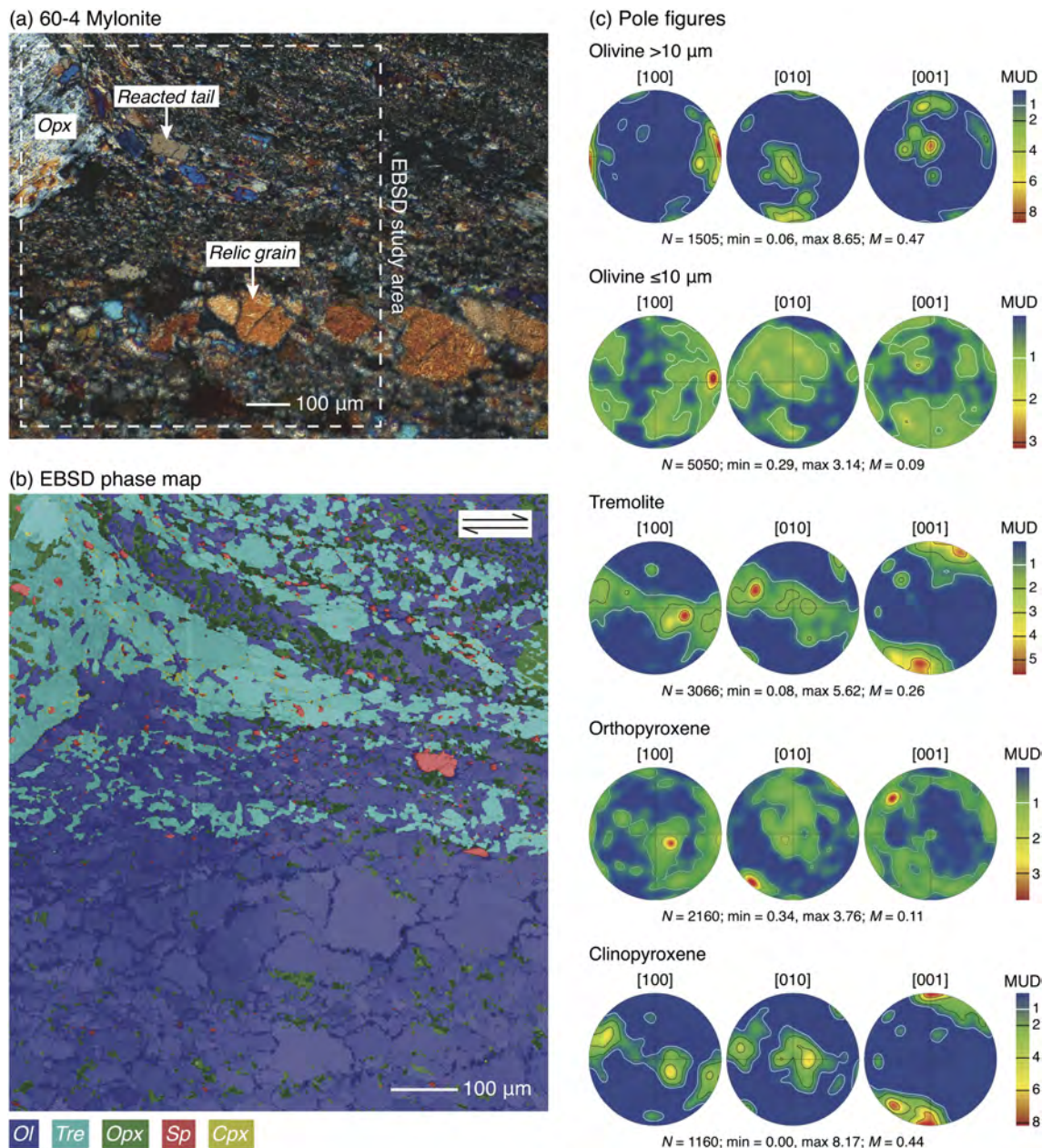
Figure 7. Deformation textures of mylonite 60-4. (a) Photomicrograph of coarse- and fine-grained bands adjacent to an orthopyroxene porphyroclast (cross-polarized light). (b) Electron backscatter diffraction (EBSD) color phase map overlain on a grayscale band contrast map, which represents relative EBSD pattern quality. (c) Pole figures for the main silicate phases, plotted as equal area lower hemisphere projections and contoured using a 15° half width based on one point per grain. N indicates the number of grains and M-index (M) quantifies fabric strength (Skemer et al., 2005). Pole figures are plotted based on data from this and an adjacent map, both collected with the foliation oriented horizontally. Data is contoured by multiples of a uniform distribution (MUD), where MUD = 1 corresponds to a random distribution of crystallographic orientations.

including the lack of an EDS detector, Warren and Hirth (2006) incorrectly mapped amphibole as pyroxene and left many grains unindexed in the fine-grained bands.

Our maps of samples 61-83 and 60-4 show that tremolite is in fact concentrated in the fine-grained bands identified by Warren and Hirth (2006). These bands are often continuous in the foliation plane with recrystallized "tails" emanating from orthopyroxene porphyroclasts, as shown in Figure 7. The grain size within the recrystallized tail appears to decrease with distance away from the clast, whereas grain size is relatively constant within the coarse-grained region below the clast (Figure 7a). The EBSD phase map shows that the
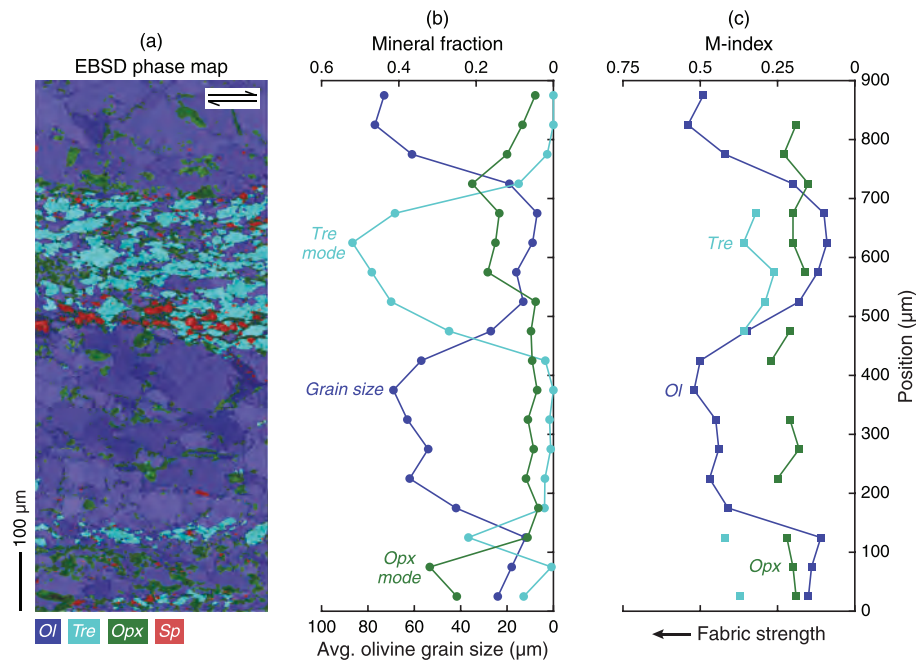
Figure 8. Electron backscatter diffraction (EBSD) profiles collected to perpendicular to mylonite foliation. (a) Phase map over greyscale band contrast map showing alternating layers of coarse-grained olivine and fine-grained olivine with tremolite, orthopyroxene, and spinel. Only trace clinopyroxene was detected within this region. (b) Average olivine grain size and secondary mineral fractions were calculated in 50 μm bins as a function of position along the profile. Olivine grain size inversely correlates with secondary phase fraction. (c) M index for olivine, tremolite, and orthopyroxene, where $M = 0$ is a random fabric and $M = 1$ is a single crystal fabric. Profiles of phase abundance and grain size were calculated by parsing data across several adjacent maps into bins with at least 100 grains in each bin for olivine and at least 50 grains in each bin for tremolite and orthopyroxene. M index values were not calculated for tremolite and orthopyroxene bins with less than the requisite number of grains.

rim of the porphyroclast is almost completely reacted to tremolite with only a small amount of orthopyroxene and fine-grained clinopyroxene (≤ 10 μm) remaining (Figure 7b). The surrounding region is a fine-grained aggregate of olivine, tremolite, and orthopyroxene, with a few larger grains of orthopyroxene and spinel. Directly below the clast and the fine-grained, tremolite-rich band, olivine grain size increases sharply and no tremolite is present. In this coarse-grained band, grain size is greatest in regions of pure olivine and decreases in regions adjacent to fine-grained orthopyroxene and spinel (Figure 7b). The grain sizes of tremolite and pyroxene within this map are <100 μm.

We analyzed olivine crystallographic textures in terms of the fine-grained (≤ 10 μm) and coarse-grained (>10 μm) fractions (Figure 7c), following the convention of Warren and Hirth (2006). Fabric strength is quantified by contouring pole figures in terms of multiples of a uniform distribution (MUD) and by the misorientation index (M index or M), which compares the distribution of misorientation angles in the data to a theoretical random distribution (Skemer et al., 2005). Fine-grained olivine shows dispersed crystallographic axis maxima, with MUD up to ~2 and $M = 0.09$. This near-random CPO is similar to that observed by Warren and Hirth (2006). Coarse-grained olivine shows a [100] maximum subparallel to the foliation and [010], [001] maxima perpendicular to the foliation with MUD > 8 and $M = 0.47$. This CPO is similar to but stronger than that observed by Warren and Hirth (2006) and is consistent with the olivine A-type fabric, which implies slip on (010)[100] (Ben Ismaïl & Mainprice, 1998; Jung et al., 2006). Tremolite and clinopyroxene show very similar CPOs defined by [100] and [010] girdles and a [001] maxima perpendicular to foliation. Orthopyroxene shows dispersed maxima and no clear fabric, with MUD ≤ 3 and $M = 0.11$.

To determine the relationships between secondary phase abundance, grain size reduction, and olivine deformation, we collected EBSD-EDS profiles perpendicular to the mylonite foliation (e.g., Figure 8a). Across the profiles, olivine grain size is inversely correlated with secondary phase fraction. The fine-grained bands

contain abundant secondary phases, mostly tremolite, which exceeds 50% abundance in several individual bins (Figure 8b). The smallest average olivine grain sizes occur when total secondary phase fractions are highest. The coarse-grained bands show relatively consistent olivine grain size, with only local grain size reduction in regions with minor amounts of fine-grained orthopyroxene.

Olivine grain size is also strongly correlated with fabric strength (Figure 8c). The coarse-grained bands show relatively consistent fabric strength with M ~0.5, which decreases sharply with grain size at the transitions to the fine-grained bands. In the finest-grained region with the most secondary phases, M reaches as low as ~0.1. Tremolite has a fabric strength of M ~0.3–0.4 in the finer-grained bands, and it is essentially absent in the coarser-grained bands. Orthopyroxene fabric strength is relatively constant across the profile and does not vary with grain size or secondary phase fraction.

5. Discussion

The Shaka peridotite mylonites preserve a complex history of hydration and brittle-ductile deformation, including FIPs, syn-deformational hydrous phases, and crosscutting fractures. Here, we argue that FIPs and syn-deformational amphibole represent evidence of fluid infiltration in the brittle-ductile transition zone. Next, we compare the stability fields of hydrous phases to a modeled fault geotherm to constrain the pressure-temperature conditions of mylonite formation and the brittle-ductile transition zone. We use these constraints, combined with our observations of mylonite grain size, to estimate the stress-strain rate conditions on the fault. Finally, we assess the potential for deep seismicity to drive fluid infiltration on OTFs via brittle fracturing in the ductile regime.

5.1. FIPs: Evidence for Deep Fluid Infiltration

We interpret the FIPs as evidence of transient episodes of fracturing and fluid infiltration under nominally ductile conditions. FIPs represent the earliest evidence of brittle deformation, as they are crosscut by both grain-scale faults in orthopyroxene (Figure 5) and serpentinized fractures (Figure 4c). Porphyroclasts contain numerous sub-parallel FIPs, possibility indicating multiple episodes of fracturing and healing under similar stress conditions (Figure 4d). FIPs are only present in the coarse-grained bands (>100 μm) and in porphyroclasts (Figure 4a), while only a few, isolated fluid inclusions are observed in grains <100 μm (Figure 4b). These observations suggest that FIPs predated development of the fine-grained bands and that they were destroyed by recrystallization during mylonite formation.

FIPs are thought to originate as mode I (tensile) cracks that open perpendicular to the least compressive stress (Lespinasse, 1999; Tuttle, 1949). Healing of fluid-filled cracks by diffusion- or dislocation-accommodated processes causes fluids to be trapped as inclusions within the fracture plane (Wanamaker et al., 1990; Wanamaker & Evans, 1985). One potential mechanism for producing fluid-filled tensile cracks in a nominally ductile rock is lithostatic pore pressure. If fluids were present on grain boundaries during ductile deformation, pore pressure may have built up enough to cause intergranular hydraulic fracturing. In this case, we would expect the fractures to trend in the direction of the maximum compressive stress, which is ~60° from the strike of the fault (Figure 1). Assuming that the mylonite foliation is parallel to the transform fault, the FIPs in porphyroclasts and large recrystallized grains trend at slighter higher angles, approximately normal to the fault strike. This does not necessarily invalidate lithostatic pore pressure an explanation for the FIPs, as the local stresses in fault zone may differ from the regional state of stress reflected by earthquake focal mechanisms.

Another possible mechanism for forming tensile cracks is earthquake rupture propagation. Theoretical and laboratory studies of earthquake rupture propagation on transform faults show that coseismic stress fields can generate sub-vertical, mode I fractures at a high angle to the fault strike (Griffith et al., 2009; Rice et al., 2005). Field studies of fault damage zones indicate that these features often act as transient pathways for fluids or melt (Di Toro et al., 2005; Mitchell et al., 2017; Mitchell & Faulkner, 2009). Mitchell and Faulkner (2009) documented abundant, sub-vertical FIPs in a continental transform fault system, which Mitchell et al. (2017) attributed to repeated cycles of coseismic damage, fluid flow, and healing. We propose that the FIPs in the Shaka mylonites also formed through coseismic damage, which implies that stress perturbations due to earthquakes on the transform fault were sufficient to fracture peridotite in the ductile regime.

The association of FIPs with brittle structures and lack of evidence for melt in these samples suggests that seawater is the fluid source. If FIPs were formed by coseismic damage, this implies that a fluid percolation network extends from the ocean floor to the brittle-ductile transition zone and is controlled by the seismic cycle. Coseismic fluid infiltration therefore may be responsible for initiating hydrolytic weakening of olivine and syn-deformational growth of tremolite. Deformation experiments on analog materials indicate that fluid inclusions in contact with grain boundaries during recrystallization can empty into grain boundaries (Schmatz & Urai, 2010, 2011). This represents a potential positive feedback mechanism between hydration and grain size reduction in the mylonites.

5.2. Syn-Deformational Hydration Reactions

Tremolite is present in the mylonites in fine-grained bands (Figure 8), recrystallized tails of orthopyroxene porphyroclasts (Figure 7), and grain-scale faults (Figures 5a and 5b). In ultramafic systems, tremolite and olivine form in a hydration reaction between orthopyroxene and clinopyroxene. For the Mg end-member minerals, the reaction is : $5En + 2Di + H_2O = Tre + Fo$, where Di is diopside, En is enstatite, Tre is tremolite, and Fo is forsterite (Chernosky et al., 1998). The microstructural relationships between tremolite and the peridotite matrix suggest that tremolite formed during dynamic recrystallization and promoted strain localization. In the high strain mylonites, we observe an inverse correlation between tremolite fraction and olivine grain size and fabric strength (Figures 8b and 8c). The destruction of the pre-existing CPO in the fine-grained bands implies that the hydration reaction promoted grain size reduction and a transition in olivine deformation mechanism to diffusion creep. We also observe a similar relationship between the fine-grained orthopyroxene fraction and olivine grain size and fabric strength, which suggests that any secondary phase can promote grain size reduction through grain boundary pinning.

Deformation experiments on amphibole and pyroxene have found that these phases are significantly stronger than olivine (Bystricky et al., 2016; Hacker & Christie, 1990; Hitchings et al., 1989), meaning that the presence of secondary phases does not directly weaken the rock. Rather, pinning of olivine grain boundaries by secondary phases promotes weakening through grain size reduction, creating the positive feedback loop necessary for intense strain localization (Poirier, 1980). Numerical modeling of deformation of two phase mixtures has shown that relatively weak, fine-grained layers tend to form in regions of phase mixing (Gardner et al., 2017). In these models, strain localization occurs when an increasing proportion of weak layers becomes interconnected, resulting in an anastomosing pattern of shear zones, similar to the texture of the high strain mylonites (Figure 3a).

The fine-grained bands in the mylonites are enriched in tremolite (Figure 8a), which suggests that hydration reactions were favored in zones of strain localization, likely because these areas contained the necessary reactants. Since fine-grained orthopyroxene is observed across both the fine- and coarse-grained bands (Figure 8a), the fine-grained layers must have also contained the other reactants, clinopyroxene and water. Hence, the distribution of pyroxenes in the proto-mylonite may have determined the pattern of strain localization. The sharp boundaries of the tremolite-rich zones also suggest that water was concentrated in zones of strain localization, which is consistent with the lack of tremolite outside the fine-grained bands.

Tremolite and clinopyroxene show similar CPOs (Figure 7c), which could indicate that the CPO was first formed in clinopyroxene and inherited by tremolite. Inheritance of a pre-existing CPO (mimetic fabric) has been documented in eclogites during the static phase transformation of pyroxene to amphibole (McNamara et al., 2012). The shared, monoclinic crystal structure of tremolite and clinopyroxene may allow tremolite to grown into (topotactic) or on top of (epitactic) the existing CPO (Putnis et al., 2006). Typically, tremolite and clinopyroxene in shear zones show CPOs with slip in the [001] direction (Díaz Aspiroz et al., 2007; Godard & van Roermund, 1995; van Roermund & Boland, 1981). In contrast, we observe slip in the [100] and [010] directions on (001). Similar textures have been interpreted to reflect syn-deformational formation of tremolite in peridotite mylonites from the Oman ophiolite (Prigent et al., 2018).

5.3. Pressure-Temperature Conditions of Ductile Deformation

The temperature conditions of mylonite deformation can be constrained from the hydrous mineralogy, but determining the pressure (depth) requires a model of the fault thermal structure as none of the minerals in spinel peridotites are pressure sensitive. The geothermal gradient of the Shaka transform fault and the faster-slipping Gofar transform fault were calculated from 3-D thermal models (Figure 9), based on the models of
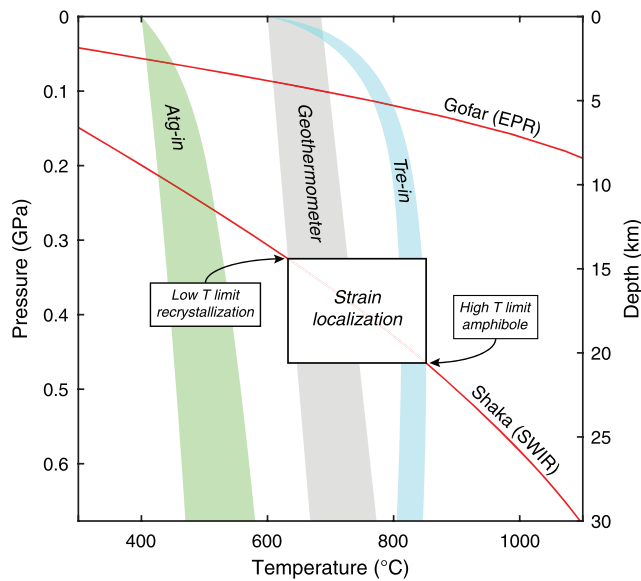
Figure 9. Pressure-temperature conditions of hydration reactions and strain localization in the Shaka mylonites (see Table 2 for details). Red lines are geotherms calculated from 3-D thermal models of the Shaka transform fault and the faster-slipping Gofar transform fault on the East Pacific Rise (Roland et al., 2012). Colored areas represent the ranges for the upper stability limits of tremolite (Tre) and antigorite serpentine (Atg) based on experimental data (Chernosky et al., 1998; Guillot et al., 2015). The grey area represents geothermometry estimates from Jaroslow et al. (1996), recalculated as a function of pressure.

Behn et al. (2007) and Wolfson-Schwehr et al. (2017). We estimate a minimum upper bound for mylonite deformation from the intersection of the experimental reaction curve for tremolite with the fault geotherm, which gives 800 °C–850 °C and 0.45 GPa (Table 2).

To estimate a lower bound for mylonite deformation, we use a geothermometer based on the closure temperature for Fe-Mg exchange between olivine-spinel pairs (Sack & Ghiorso, 1991). In previous analyses of the Shaka mylonites, Jaroslow et al. (1996) estimated a temperature range of 580–670 °C from olivine-spinel neoblasts, which represents the low temperature limit of recrystallization . The calculation by Jaroslow et al. (1996) used an earlier version of the Sack and Ghiorso (1991) thermometer with a pressure of either 1 bar or 1 kbar (0.1 GPa), which is too low for an oceanic crust geotherm. We used the Jaroslow et al. (1996) mineral compositions and the Sack and Ghiorso (1991) thermometer to recalculate temperature as a function of pressure. In Figure 9, we use this thermometry estimate to a lower bound of 650–750 °C and 0.35-0.4 GPa for ductile deformation on the fault. This constrains the conditions of mylonite formation (strain localization) to ~650–850 °C and 0.35–0.45 GPa, which corresponds to ~15 to 21 km depth on the fault.

5.4. Deformation Mechanism Maps

The microstructures of the Shaka mylonites record the deformation mechanisms and stress-strain rate conditions of the fault. To understand deformation within the brittle-ductile transition zone, we consider the evolution of the fault microstructure from protolith to mylonite. We assume that the protolith is a typical upper mantle peridotite, which field studies indicate has an olivine grain size of ~0.5–5 mm (Achenbach et al., 2011; Hansen & Warren, 2015; Warren et al., 2009). This is consistent with the size of porphyroclasts in the Shaka mylonites (Figures 3a and 3b). Assuming that shear zone deformation extends to the base of the lithosphere, the high P-T limit for deformation is constrained by the mantle potential temperature. For the ridge segment adjacent to the Shaka Transform Fault, Dalton et al. (2014) estimated a potential temperature of ~1380 °C, which corresponds to a pressure (depth) of ~1.5 GPa (70 km) based on the fault thermal structure (Figure 9). For the mylonites, the average deformation conditions estimated in 4section 5.3 are 750 °C and 0.4 GPa (18 km), slightly revised from the previous estimate of 700 °C and 0.4 GPa from Warren and Hirth (2006).

Figure 10 shows olivine deformation mechanism maps for the protolith and mylonite, calculated using the flow law constitutive equations and parameters given in the Appendix (Table A2). Although we interpret deformation in the mylonites as a multiphase process, with secondary phases playing an important role in strain localization, these calculations only consider a pure olivine system. At present, flow laws for olivine-pyroxene and/or olivine-amphibole mixtures are not available, though experiments have been

Table 2
Estimated P-T Conditions for Ductile Deformation in the Shaka Transform Fault Mylonites

Constraint	Basis	Temperature	Pressure	Reference
Antigorite-in	Experimental reaction curve	450 °C–550 °C	0.25 GPa	Guillot et al. (2015)
Lower bound for recrystallization	Geothermometry, fault geothem	650–750 GPa	0.35 GPa	Jaroslov et al. (1996) This study (Figure 9)
Upper bound for mylonite deformation	Tremolite-in, fault geotherm	800 °C–850 °C	0.45 GPa	This study (Figure 9)
Tremolite-in	Experimental reaction curve	800 °C–850 °C	0.45 GPa	Chernosky et al. (1998)
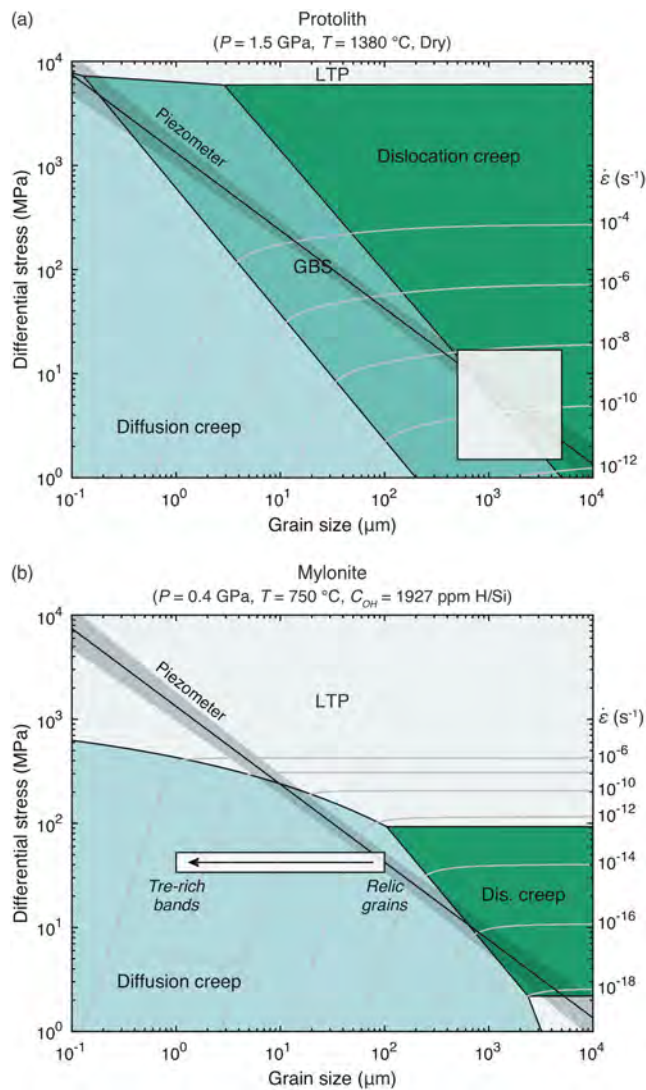
Figure 10. Olivine deformation mechanism maps calculated using the flow laws and parameters in Table A2. Colored regions separated by black lines indicate the dominant olivine deformation mechanism for a given combination of grain size and differential stress. Light grey lines represent contours of constant strain rate. (a) Protolith conditions — dry deformation at 1.5 GPa and 1380 °C. Grain size is estimated as 0.5–5 mm (grey box), which implies deformation at low differential stress by a combination of grain boundary sliding and dislocation creep. (b) Mylonite conditions — wet deformation at 0.4 GPa and 750 °C. Grain size in the coarse-grained, monophase olivine layers is ~100 μm, which implies deformation by a combination of diffusion creep and dislocation creep. The formation of the fine-grained, tremolite-rich bands (1–10 μm) through strain localization is assumed to have occurred under iso-stress conditions (arrow in grey box). LTP — low temperature plasticity.

conducted for olivine-pyroxene mixtures that are more iron rich than the mantle (Tasaka et al., 2013). As the extrapolation of this flow law to mantle compositions is unknown, the pure olivine flow law remains the best option for assessing the impacts of strain localization and hydration on fault rheology. For the protolith, we assumed dry conditions (Figure 10a) and for the mylonite we assumed that olivine was saturated with water (Figure 10b). We used a water content (C_{OH}) of 2,175-ppm H/Si, calculated from the experimentally defined relationship for the storage capacity of olivine as a function pressure and temperature (Hirschmann et al., 2005). A key difference between the wet and dry maps is that the dislocation-accommodated grain boundary sliding (GBS) field is replaced by diffusion creep and low-temperature plasticity (LTP) at the conditions of mylonite deformation. While GBS is active at grain sizes ~100 μm to 5 mm at the protolith conditions, when olivine is hydrated, diffusion creep is the weakest deformation mechanism at grain sizes ~1 μm to 1 mm.

To estimate the differential stress during deformation, we use the recrystallization piezometer for olivine, which provides an empirical relationship between stress and grain size, based on experimental observations (Karato et al., 1980; Van der Wal et al., 1993). The protolith grain size (0.5–5 mm) corresponds to low differential stresses of <10 MPa, which plots at the intersection of the GBS and dislocation creep fields, indicating an equal contribution from both mechanisms and a strain rate of ~10^{-8}–10^{-12} s^{-1} (Figure 10a).

In the mylonites, olivine grain size varies from ~100 μm in the coarser-grained bands to ~1 μm in the tremolite-rich, fine-grained bands. At 100 μm, the recrystallization piezometer plots in the diffusion creep field, close to the field boundary with dislocation creep (Figure 10b). This implies deformation at moderate differential stresses of ~40–60 MPa and a similar strain rate as the protolith, ~10^{-12} s^{-1}. The recrystallization piezometer is only calibrated for monophase olivine aggregates, so we assume grain size reduction occurred under iso-stress conditions in order to estimate the strain rate in the fine-grained, multiphase bands. If directly applied to fine-grained bands, the recrystallization piezometer predicts unreasonably high stresses (>1 GPa) and strain rates (>10^{-5} s^{-1}). At the differential stress estimated for the coarse-grained bands (40–60 MPa), olivine in fine-grained bands (1–10 μm) is expected to deform at a fast, but plausible, strain rate of ~10^{-7}–10^{-9} s^{-1} (Figure 10b). The 2 orders of magnitude reduction in grain size between the fine- and coarse-grained bands result in an increase in strain rate of approximately 5 orders of magnitude.

5.5. Feedbacks Between Hydration, Strain Localization, and Olivine Deformation Mechanisms

Constraints from the mineralogy, microstructures, and deformation textures of the mylonites enable us to develop a model for hydration and strain localization on the Shaka transform fault. Previous analysis of ultra-mylonite 61-83 by Warren and Hirth (2006) focused on three micro-structural observations to explain the ductile deformation of the mylonites: (i) absence of a CPO in the finest recrystallized grains; (ii) presence of a CPO in relatively coarse recrystallized grains; and (iii) preservation of porphyroclasts. Our analysis confirms these observations and also reveals syn-deformational hydration in the form of FIPs and amphibole. We hypothesize that fluid infiltration into the brittle-ductile transition zone initiated a positive feedback loop between hydration and deformation that promoted strain localization through hydrolytic weakening and amphibole formation (Figure 11).
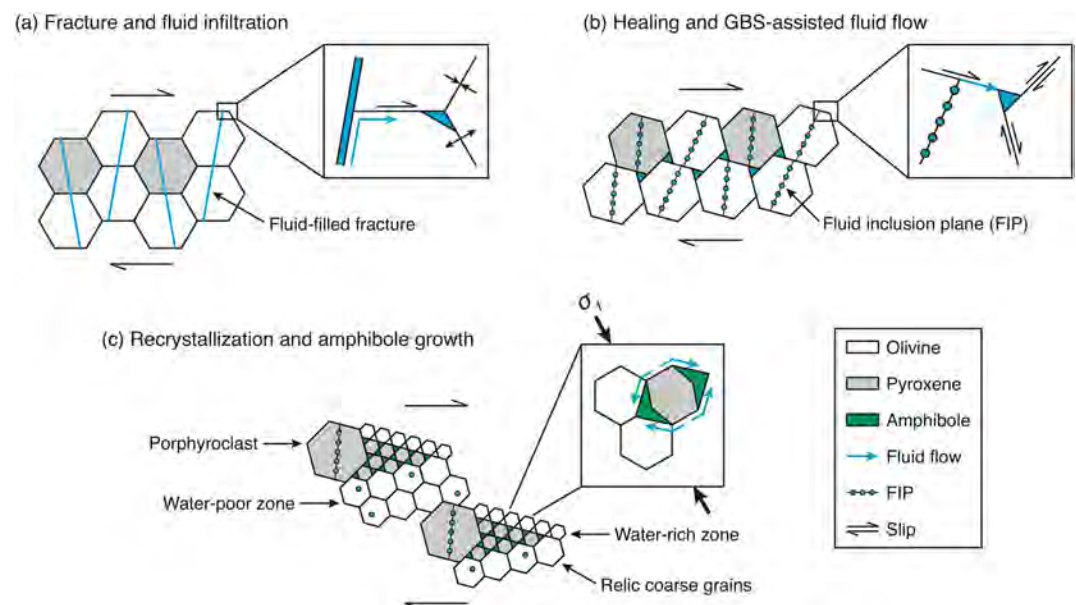
Figure 11. Model for fluid infiltration, strain localization, and hydrous phase growth. (a) Stress perturbations induce fracture of millimeter-scale grains of olivine and pyroxene (protolith) at nominally ductile conditions, resulting in fluid infiltration. Healing between brittle events may push fluids into grain boundaries (inset), while fluids within grains are preserved as fluid inclusion planes (FIPs). (b) Further deformation of the protolith by grain boundary sliding (GBS) may direct fluid flow through dilatational spaces into rapidly deforming layers. (c) Fluid flow into the pressure shadows of pyroxene porphyroclasts results in hydrolytic weakening and tremolite growth, creating a positive feedback loop for strain localization. Deformation in diffusion creep may facilitate tremolite growth through solution transfer along olivine-pyroxene phase boundaries (inset).

The first stage of our model is based on the assumption that fracturing and fluid infiltration were responsible for initial hydration of the protolith (Figure 11a). The presence of FIPs in both olivine and pyroxene porphyroclasts (Figures 4 and 5) suggests that fluid-filled fractures formed and healed prior to grain size reduction, particularly since FIPs are largely absent in recrystallized grains (Figure 4b). If fractures extended across grains, fluids may have been transported into grain boundaries and triple junctions (Figure 11a, inset).

In the second stage, deformation of the protolith by GBS (Figure 10a) causes fluids to be transported through a network of local dilatant zones (Figure 11b). This process, termed "creep cavitation," occurs when grain boundary slip cannot be fully accommodated by other deformation mechanisms, resulting in the opening and closing of intergranular pathways for fluid flow (Kassner & Hayes, 2003; Fusseis et al., 2009; Condit & Mahan, 2018; Figure 11b, inset). The tendency of GBS to promote fluid flow via creep cavitation may result from fluids being drawn into rapidly deforming zones, making them weaker and thus causing them to deform faster.

In the final stage, fluid flow into rapidly deforming zones and porphyroclast pressure shadows results in hydrolytic weakening and tremolite growth, creating a positive feedback loop for strain localization (Figure 11c). Recent studies of natural and experimental mylonites also indicate that fluid flow and hydration reactions are concentrated in porphyroclast pressure shadows, causing weakening and grain boundary pinning of olivine (Précigout et al., 2017; Précigout & Stünitz, 2016; Spruzeniece & Piazolo, 2015). In the Shaka mylonites, coupling between fluid flow, hydration reactions, and deformation may explain the sharp transitions in olivine fabric and grain size at the boundaries of the fine-grained bands (Figure 8). If strain localization was driven by a gradient in fluid content, alternating high- and low-strain layers at various length scales (Figures 3 and 8) may represent relatively water-rich and water-poor zones.

GBS may be responsible for initiating strain localization in the protolith by promoting phase mixing and fluid flow into rapidly deforming zones. Prior to hydration, strain localization was likely initiated by grain boundary pinning of olivine by pyroxene. Once water was added to the peridotite, tremolite may have preferentially formed in the rapidly deforming, pyroxene-rich zones, resulting in additional grain boundary

pinning of olivine. Tremolite growth may have also been enhanced by solution transfer at olivine-pyroxene phase boundaries (Figure 11c, inset). The negative correlation of olivine fabric strength and hydrous phase fraction (Figure 8b) suggests an increasing contribution of diffusion creep in the fine-grained bands, as deformation in diffusion creep yields randomly oriented grains. Similar patterns of grain size reduction, fabric evolution and amphibole growth have been observed in peridotite mylonites from the Ronda massif (Précigout et al., 2017). In these samples, the fine-grained bands are relatively clinopyroxene-rich and amphibole-poor compared to equivalent features in the Shaka mylonites, possibility indicating a lesser degree of hydration.

In summary, we propose that the Shaka mylonites formed by a feedback between hydration, strain localization, and olivine deformation. Grain boundary pinning of olivine by pyroxene was likely responsible for initiating strain localization in the dry protolith. Fracturing and fluid infiltration under ductile conditions resulted in the formation of FIPs and distributed fluids along grain boundaries. Fluid and mass transfer into rapidly deforming zones and porphyroclast pressure shadows set up the conditions for hydrous phase formation and grain size reduction, causing a transition in olivine deformation mechanism from GBS to diffusion creep. Solution transfer during diffusion creep may have promoted tremolite growth, which is responsible for additional grain boundary pinning of olivine in relatively water-rich zones.

### 5.6. Implications for the Strength and Seismicity of OTFs

The presence of syn-deformational and post-deformational hydration features in the Shaka mylonites has important implications for the strength and seismic properties of OTFs. Our results suggest that brittle failure occurred on the Shaka transform fault at temperatures typically associated with ductile deformation of peridotite. The association of hydration with brittle structures (FIPs) suggests that coseismic damage may have been responsible for deep fluid infiltration into the brittle-ductile transition zone. This runs counter to conventional models of OTFs but agrees with recent observations of deep seismicity on faster slipping OTFs.

Estimates of the depth extent of brittle deformation on OTFs have previously been derived from several lines of evidence. Global teleseismic surveys of earthquake focal depths in conjunction with numerical models of fault thermal structure have concluded that earthquakes are confined to depths shallower than the 600 °C isotherm (Abercrombie & Ekström, 2001; Chen & Molnar, 1983; Engeln et al., 1986; McKenzie et al., 2005). Laboratory deformation experiments on olivine aggregates also indicate that the transition from brittle to ductile behavior occurs around 600 °C at lithospheric strain rates (Boettcher et al., 2007). Finally, Jaroslow et al. (1996) estimated ~600 °C for the lower temperature limit for ductile deformation based on mineral thermometry of OTF mylonites. Together, these constraints underlie the assumption that brittle deformation and seawater infiltration on OTFs are limited to depths shallower than the 600 °C isotherm. However, the lower temperature limit for ductile deformation in the mylonites is not necessarily the same as the upper temperature limit for brittle deformation, as demonstrated by the presence of FIPs in the porphyroclasts. This may be explained by strain rate dependence of the thermal limit of brittle deformation observed in laboratory deformation experiments (Boettcher et al., 2007). Brittle failure is limited to 600 °C at lithospheric strain rates, 10^{-12}–10^{-15} s^{-1}, but occurs at ~900 °C at the strain rates estimated for the mylonite, ~10^{-7}–10^{-9} s^{-1} (Figure 10b).

Brittle failure at >600 °C is also observed geophysically. Recent ocean-bottom seismic surveys of transform faults on the East Pacific Rise have documented earthquakes extending to depths beyond the 1000 °C isotherm in modeled thermal structure (Froment et al., 2014; McGuire et al., 2012; Roland et al., 2012; Wolfson-Schwehr et al., 2014). On the Gofar transform fault, Roland et al. (2012) found that large mainshock events and associated aftershocks are restricted to temperatures <600 °C, while foreshocks extend to depths corresponding to ~1100 °C. This suggests that the depth of the brittle-ductile transition varies during the seismic cycle of OTFs. In the context of the Shaka mylonites, the deep foreshocks provide a potential mechanism for fluid infiltration, in which preseismic and coseismic brittle deformation create a transient fluid percolation network that is healed by ductile deformation during interseismic periods (Figure 12).

Evidence of seismicity at equivalent temperatures to our estimates for FIP formation and hydrous phase growth suggests that the processes recorded by the Shaka mylonites may be characteristic of OTFs in
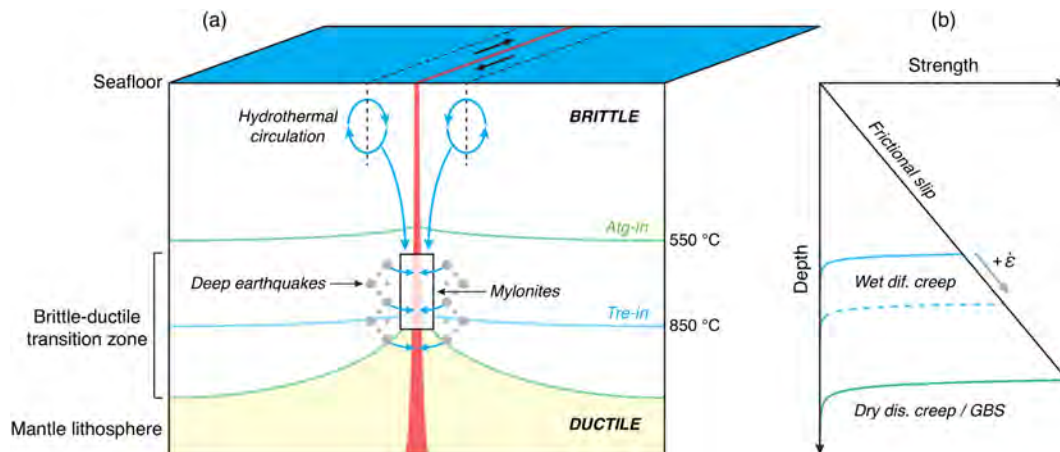
Figure 12. Hydrologic and deformation processes on oceanic transform faults based on constraints from the Shaka mylonites. (a) Coseismic damage from deep earthquakes creates a fluid infiltration pathway that connects shallow hydrothermal circulation to the brittle-ductile transition zone. Seawater in the fault zone promotes strain localization through hydrolytic weakening and hydrous phase growth. (b) Hydration and strain localization results in a transition in olivine deformation mechanism from dry dislocation creep and grain boundary sliding (GBS) at the deepest extent of the brittle-ductile transition to wet diffusion creep at the shallowest extent.

general. Ocean-bottom seismic data are not available for Shaka, so we need to consider differences in thermal structure in order to connect observations of deep seismicity to mylonite deformation. The lateral offsets of the Shaka (210 km) and Gofar (190 km) transform faults are similar, but Shaka has a slip rate of ~13 mm/year, whereas Gofar slips nearly an order of magnitude faster at 124 mm/year (Wolfson-Schwehr & Boettcher, 2019). As a result, the faults have very different thermal structure as a function of depth (Figure 9). At Shaka, 600 °C–1100 °C corresponds to ~14-30 km depth, compared to ~4-8 km at Gofar. This implies that the equivalent brittle-ductile transition zone at Gofar occurs over a much narrower and shallower depth range. If temperature is in fact the primary control on fault zone rheology, Shaka and Gofar may undergo similar deformation and hydration processes at different depths.

Our estimates of the mylonite deformation conditions also provides insights into the relationship between fault zone structure and OTF seismicity. The estimated strain rate in the fine-grained bands deforming by wet diffusion creep is $\sim 10^{-7}$–$10^{-9}\,s^{-1}$ (Figure 10b), which falls within the range for estimates of post seismic creep in the oceanic lithosphere (Montési & Hirth, 2003; Warren & Hirth, 2006). If we assume that the fine-grained bands in the ultra-mylonite and mylonite represent the rheology of a high-strain fault core, these high strain rates would allow stress to relax continuously through creep, while the surrounding coarse-grained material accumulates stress (Bercovici & Ricard, 2016). Repeated fracturing of the coarse-grained material would result in the formation of a fault damage zone, which may be represented by the two altered mylonites. At >600 °C, the fault core is unlikely to accumulate sufficient elastic strain energy for brittle failure, which implies that episodes of fracturing and fluid infiltration must have occurred before strain localization (i.e., Figure 11a). Therefore, we consider the fault core as the narrowest and shallowest extent of the brittle-ductile transition zone (Figure 12a).

Our results demonstrate that deep fluid infiltration on OTFs strongly impacts fault zone rheology. Comparing ductile flow flaws with the relationship for fault frictional strength suggests that the brittle-ductile transition zone represents the evolution of fault zone deformation from the protolith to mylonite (Figure 12b). This implies that the change in olivine deformation mechanisms due to hydration and strain localization determines the structure of the brittle-ductile transition zone. Therefore, along-strike variations in the depth extent of OTF seismicity (e.g., Froment et al., 2014; McGuire et al., 2012) may be explained by differences in fault hydrology, which result in differences in fault rheology.

6. Conclusions

Peridotite mylonites from the Shaka transform fault preserve evidence of fluid infiltration and syn-deformational hydration reactions. FIPs contained within relic coarse grains record repeated cycles of

fracture, fluid infiltration, and healing. The mylonite fabric is defined by anastomosing bands of extreme grain size reduction, which show syn-deformational growth of tremolite amphibole and loss of the pre-existing CPO. The association of FIPs with brittle structures and the abundance of amphibole suggest that seawater is the fluid source. Olivine grain size and fabric strength vary inversely with secondary phase content across the deformational banding, indicating that grain boundary pinning by both pyroxene and tremolite were responsible for strain localization and a transition in the olivine deformation mechanism from GBS to diffusion creep. Comparing conditions of tremolite stability and geothermometry estimates on recrystallized grains to the fault geotherm indicates that strain localization occurred at ~650–850 °C (15-21 km). For the mylonite grain sizes (1–10 μm), the olivine recrystallization piezometer predicts rapid strain rates of 10^{-7}–10^{-9} s^{-1}, which is on order of what is expected for postseismic creep in the oceanic lithosphere.

Our analysis of the mylonites has several important implications for the behavior of OTFs. First, estimates for the thermal limit of brittle deformation and hydration in the mylonites are consistent with observations of earthquakes on EPR transforms at >600 °C, which suggests that the deep hydrologic cycle on OTFs is driven by seismicity. Observations of brittle deformation and hydration at temperatures where ductile deformation is expected suggests that seawater infiltration extends to much greater depths than previously thought. Second, the rapid strain rates estimated for the mylonites imply that the high strain regions of the fault may be able to continuously relax stress through diffusion creep at hydrous conditions. Finally, the relationships between hydration, strain localization, and olivine deformation indicate that the depth of the brittle-ductile transition zone on OTFs is spatially dependent on fault zone rheology and temporally dependent on the seismic cycle.

Appendix A.

Table A2 provides the flow law constitutive parameters used in the deformation mechanism maps (Figure 10). The form of the flow laws for diffusion creep, GBS, and dislocation creep (Hirth & Kohlstedt, 2003) is:

$$\dot{\varepsilon} = A\sigma^n d^p C_{OH}^r e^{\left[-\frac{E+PV}{RT}\right]} \tag{A1}$$

where A is the combined pre-exponential factor, σ is the differential stress, n is the stress exponent, d is grain size, p is the grain size exponent, C_{OH} is water concentration and r is the water concentration exponent, E is the activation energy, V is the activation volume, and R is the universal gas constant. The value of A has been adjusted from the original references to account for updated estimates of the water content in the experimental samples (i.e., Bell et al., 2003). The flow law for dry LTP (Mei et al., 2010) is:

$$\dot{\varepsilon} = A\sigma^n e^{\left[-\frac{E}{RT}\left(1-\sqrt{\frac{\sigma}{\sigma_P}}\right)\right]} \tag{A2}$$

where σ_P is the Peierels stress. The flow law for wet LTP (Katayama & Karato, 2008) is:

$$\dot{\varepsilon} = A\sigma^n C_{OH}^r e^{\left[-\frac{E}{RT}\left(1-\frac{\sigma}{\sigma_P}\right)^p\right]^q} \tag{A3}$$

where p and q are nondimensional parameters that describe dislocation motion.

Table A1
Bulk Rock Compositions for Shaka Peridotite Mylonites

	Unnormalized Major Elements (wt%)											
ID	SiO$_2$	TiO$_2$	Al$_2$O$_3$	FeO	MnO	MgO	CaO	Na$_2$O	K$_2$O	P$_2$O$_5$	Loss on Ignition (wt%)	Reference
61-83	43.35	0.03	2.07	8.22	0.13	41.27	1.90	0.10	0.01	0.00	2.0	Craddock et al. (2013)
60-4	43.16	0.041	2.04	7.88	0.127	40.14	1.99	0.18	0.01	0.006	3.8	This study
60-7	42.72	0.032	2.09	7.88	0.117	39.50	1.74	0.16	0.02	0.017	4.7	This study
60-5	43.80	0.094	3.00	7.01	0.121	37.63	3.02	0.24	0.01	0.006	5.0	This study

Table A2
Flow Law Constitutive Parameters Used in Deformation Mechanism Maps (Figure 10)

Mechanism	n	p	q	r	A	E (kJ/mol)	V (10^{-6} m^3/mol)	σ_p (GPa)	References
Dry diffusion creep	1	−3	—	—	1.50E + 09	375	2	—	Hirth and Kohlstedt (2003)
	—	—	—	—	3.98E + 07	—	—	—	Hansen et al. (2011)
Dry GBS	2.9	−0.7	—	—	5.01E + 04	445	18	—	Hansen et al. (2011)
Dry dislocation creep	3.5	0	—	—	1.10E + 05	520	14	—	Hirth and Kohlstedt (2003)
Dry LTP	2	0.5	1	—	1.40E − 07	320	0	5.9	Mei et al. (2010)
Wet diffusion creep	1	−3	—	1	4.00E + 05	335	4	—	Hirth and Kohlstedt (2003)
Wet GBS	3	−1	—	1.25	1.29E + 01	423	17.6	—	Ohuchi et al. (2015)
Wet dislocation creep	3.5	0	—	1.2	3.00E + 01	480	11	—	Hirth and Kohlstedt (2003)
Wet LTP	2	0.75	1	—	1.26E + 07	518	—	2.1	Katayama and Karato (2008)

References

Abercrombie, R. E., & Ekström, G. (2001). Earthquake slip on oceanic transform faults. *Nature*, *410*(6824), 74–77. https://doi.org/10.1038/35065064

Achenbach, K. L., Cheadle, M. J., Faul, U., Kelemen, P., & Swapp, S. (2011). Lattice-preferred orientation and microstructure of peridotites from ODP Hole 1274A (15°39′N), Mid-Atlantic Ridge: Testing models of mantle upwelling and tectonic exhumation. *Earth and Planetary Science Letters*, *301*(1–2), 199–212. https://doi.org/10.1016/j.epsl.2010.10.041

Barton, C. A., Zoback, M. D., & Moos, D. (1995). Fluid flow along potentially active faults in crystalline rock. *Geology*, *23*, 683–686.

Behn, M. D., Boettcher, M. S., & Hirth, G. (2007). Thermal structure of oceanic transform faults. *Geology*, *35*(4), 307. https://doi.org/10.1130/G23112A.1

Bell, D. R., Rossman, G. R., Maldener, J., Endisch, D., & Rauch, F. (2003). Hydroxide in olivine: A quantitative determination of the absolute amount and calibration of the IR spectrum. *Journal of Geophysical Research - Solid Earth*, *108*(B2), 1–9. https://doi.org/10.1029/2001JB000679

Ben Ismaïl, W., & Mainprice, D. (1998). An olivine fabric database: An overview of upper mantle fabrics and seismic anisotropy. *Tectonophysics*, *296*, 145–157. https://doi.org/10.1016/S0040-1951(98)00141-3

Bercovici, D., & Ricard, Y. (2016). Grain-damage hysteresis and plate tectonic states. *Physics of the Earth and Planetary Interiors*, *253*, 31–47. https://doi.org/10.1016/j.pepi.2016.01.005

Bodinier, J. L., Godard, M., Holland, H. D., & Turekian, K. K. (2014). *Treatise on geochemistry*, (Vol. 2). Oxford, UK: Elsevier Science.

Boettcher, M. S., Hirth, G., & Evans, B. (2007). Olivine friction at the base of oceanic seismogenic zones. *Journal of Geophysical Research*, *112*, B01205. https://doi.org/10.1029/2006JB004301

Bonatti, E., Brunelli, D., Buck, W. R., Cipriani, A., Fabretti, P., Ferrante, V., & Ligi, M. (2005). Flexural uplift of a lithospheric slab near the Vema transform (Central Atlantic): Timing and mechanisms. *Earth and Planetary Science Letters*, *240*(3–4), 642–655. https://doi.org/10.1016/j.epsl.2005.10.010

Bonatti, E., Ligi, M., Gasperini, L., Peyve, A., Raznitsin, Y., & Chen, Y. J. (1994). Transform migration and vertical tectonics at the Romanche Fracture Zone, equatorial Atlantic. *Journal of Geophysical Research*, *99*(B11), 779–802. https://doi.org/10.1029/94JB01178

Bystricky, M., Lawlis, J., Mackwell, S., Heidelbach, F., & Raterron, P. (2016). High-temperature deformation of enstatite aggregates. *Journal of Geophysical Research: Solid Earth*, *121*, 6384–6400. https://doi.org/10.1002/2016JB013011

Cannat, M., Bideau, D., & Hébert, R. (1990). Plastic deformation and magmatic impregnation in serpentinized ultramafic rocks from the Garrett transform fault (East Pacific Rise). *Earth and Planetary Science Letters*, *101*(2–4), 216–232. https://doi.org/10.1016/0012-821X(90)90155-Q

Cannat, M., & Seyler, M. (1995). Transform tectonics, metamorphic plagioclase and amphibolitization in ultramafic rocks of the Vema transform fault (Atlantic Ocean). *Earth and Planetary Science Letters*, *133*(3–4), 283–298. https://doi.org/10.1016/0012-821X(95)00078-Q

Chen, W.-P., & Molnar, P. (1983). Focal depths of intracontinental and intraplate earthquakes and their implications for the thermal and mechanical properties of the lithosphere. *Journal of Geophysical Research*, *88*(B5), 4183–4214.

Chernosky, J. V. Jr., Berman, R. G., & Jenkins, D. M. (1998). The stability of tremolite: New experimental data and a thermodynamic assessment. *American Mineralogist*, *83*, 726–738.

Cipriani, A., Bonatti, E., Seyler, M., Brueckner, H. K., Brunelli, D., Dallai, L., & Turrin, B. D. (2009). A 19 to 17 Ma amagmatic extension event at the Mid-Atlantic Ridge: Ultramafic mylonites from the Vema Lithospheric Section. *Geochemistry, Geophysics, Geosystems*, *10*, Q10011. https://doi.org/10.1029/2009GC002534

Condit, C. B., & Mahan, K. H. (2018). Fracturing, fluid flow and shear zone development: Relationships between chemical and mechanical processes in Proterozoic mafic dykes from southwestern Montana, USA. *Journal of Metamorphic Geology*, *36*(2), 195–223. https://doi.org/10.1111/jmg.12289

Craddock, P. R., Warren, J. M., & Dauphas, N. (2013). Abyssal peridotites reveal the near-chondritic Fe isotopic composition of the Earth. *Earth and Planetary Science Letters*, *365*, 63–76. https://doi.org/10.1016/j.epsl.2013.01.011

Dalton, C. A., Langmuir, C. H., & Gale, A. (2014). Geophysical and geochemical evidence for deep temperature variations beneath mid-ocean ridges. *Science*, *344*, 80–83. https://doi.org/10.1126/science.1249466

Kreemer, C., Holt, W. E., & Haines, A. J. (2003). An integrated global model of present-day plate motions and plate boundary deformation. *Geophysical Journal International*, *154*(1), 8–34. https://doi.org/10.1046/j.1365-246X.2003.01917.x

Di Toro, G., Nielsen, S., & Pennacchioni, G. (2005). Earthquake rupture dynamics frozen in exhumed ancient faults. *Nature*, *436*(7053), 1009–1012. https://doi.org/10.1038/nature03910

Díaz Aspiroz, M., Lloyd, G. E., & Fernández, C. (2007). Development of lattice preferred orientation in clinoamphiboles deformed under low-pressure metamorphic conditions. A SEM/EBSD study of metabasites from the Aracena metamorphic belt (SW Spain). *Journal of Structural Geology*, *29*(4), 629–645. https://doi.org/10.1016/j.jsg.2006.10.010

Dick, H. J. B., Lin, J., & Schouten, H. (2003). An ultraslow-spreading class of ocean ridge. *Nature*, *426*(6965), 405–412. https://doi.org/10.1038/nature02128

Dick, H. J. B., Fisher, R. L., & Bryan, W. B. (1984). Mineralogic variability of the uppermost mantle along mid-ocean ridges. *Earth and Planetary Science Letters*, *69*(1), 88–106. https://doi.org/10.1016/0012-821X(84)90076-1

Dziewoński, A. M., Chou, T.-A., & Woodhouse, J. H. (1981). Determination of earthquake source parameters from waveform data for studies of global and regional seismicity. *Journal of Geophysical Research - Solid Earth*, *86*(B4), 2825–2852. https://doi.org/10.1029/JB086iB04p02825

Ekström, G., Nettles, M., & Dziewoński, A. M. (2012). The global CMT project 2004–2010: Centroid-moment tensors for 13,017 earthquakes. *Physics of the Earth and Planetary Interiors*, *200–201*, 1–9. https://doi.org/10.1016/j.pepi.2012.04.002

Engeln, J. F., Wiens, D. A., & Stein, S. (1986). Mechanisms and depths of Atlantic transform earthquakes intersections. *Journal of Geophysical Research*, *91*(5), 548–577. https://doi.org/10.1029/JB091iB01p00548

Farmer, H. G., & Dick, H. J. B. (1981). *Description of W.H.O.I. rock dredge samples. WHOI Technical Report* (Vol. 3).

Froment, B., Mcguire, J. J., van der Hilst, R. D., Gouedard, P., Roland, E. C., Zhang, H., & Collins, J. A. (2014). Imaging along-strike variations in mechanical properties of the Gofar transform fault, East Pacific Rise. *Journal of Geophysical Research: Solid Earth*, *119*, 7175–7194. https://doi.org/10.1002/2014JB011270

Fusseis, F., Regenauer-Lieb, K., Liu, J., Hough, R. M., & De Carlo, F. (2009). Creep cavitation can establish a dynamic granular fluid pump in ductile shear zones. *Nature*, *459*(7249), 974–977. https://doi.org/10.1038/nature08051

Gardner, R., Piazolo, S., Evans, L., & Daczko, N. (2017). Patterns of strain localization in heterogeneous, polycrystalline rocks—A numerical perspective. *Earth and Planetary Science Letters*, *463*, 253–265. https://doi.org/10.1016/j.epsl.2017.01.039

Godard, G., & van Roermund, H. L. M. (1995). Deformation-induced clinopyroxene fabrics from eclogites. *Journal of Structural Geology*, *17*(10), 1425–1443. https://doi.org/10.1016/0191-8141(95)00038-F

Griffith, W. A., Rosakis, A., Pollard, D. D., & Ko, C. W. (2009). Dynamic rupture experiments elucidate tensile crack development during propagating earthquake ruptures. *Geology*, *37*(9), 795–798. https://doi.org/10.1130/G30064A.1

Guillot, S., Schwartz, S., Reynard, B., Agard, P., & Prigent, C. (2015). Tectonic significance of serpentinites. *Tectonophysics*, *646*, 1–19. https://doi.org/10.1016/j.tecto.2015.01.020

Hacker, B. R., & Christie, J. M. (1990). Brittle/ductile and plastic/cataclastic transitions in experimentally deformed and metamorphosed amphibolite. *AGU Monograph*, *56*, 127–147. https://doi.org/doi:10.1029/GM056p0127

Hansen, L. N., & Warren, J. M. (2015). Quantifying the effect of pyroxene on deformation of peridotite in a natural shear zone. *Journal of Geophysical Research: Solid Earth*, *120*, 2717–2738. https://doi.org/10.1002/2014JB011584

Hansen, L. N., Zimmerman, M. E., & Kohlstedt, D. L. (2011). Grain boundary sliding in San Carlos olivine: Flow law parameters and crystallographic-preferred orientation. *Journal of Geophysical Research - Solid Earth*, *116*(8), 1–16. https://doi.org/10.1029/2011JB008220

Heidbach, O., Rajabi, M., Cui, X., Fuchs, K., Müller, B., Reinecker, J., & Zoback, M. (2018). The World Stress Map database release 2016: Crustal stress pattern across scales. *Tectonophysics*, *744*(July), 484–498. https://doi.org/10.1016/j.tecto.2018.07.007

Hekinian, R., Bideau, D., Cannat, M., Francheteau, J., & Hébert, R. (1992). Volcanic activity and crust-mantle exposure in the ultrafast Garrett transform fault near 13°28′S in the Pacific. *Earth and Planetary Science Letters*, *108*(4), 259–275. https://doi.org/10.1016/0012-821X(92)90027-S

Hirschmann, M. M., Aubaud, C., & Withers, A. C. (2005). Storage capacity of H_2O in nominally anhydrous minerals in the upper mantle. *Earth and Planetary Science Letters*, *236*, 167–181. https://doi.org/10.1016/j.epsl.2005.04.022

Hirth, G., & Kohlstedt, D. (2003). Rheology of the upper mantle wedge: A view from the experimentalists. *Inside the Subduction Factory AGU Monograph*, *138*, 83–105.

Hitchings, R. S., Paterson, M. S., & Bitmead, J. (1989). Effects of iron and magnetite additions in olivine-pyroxene rheology. *Physics of the Earth and Planetary Interiors*, *55*, 277–291. https://doi.org/10.1016/0031-9201(89)90076-9

Jaroslow, G. E., Hirth, G., & Dick, H. J. B. (1996). Abyssal peridotite mylonites: Implications for grain-size sensitive flow and strain localization in the oceanic lithosphere. *Tectonophysics*, *256*, 17–37. https://doi.org/10.1016/0040-1951(95)00163-8

Johnson, D. M., Hooper, P. R., & Conrey, R. M. (1999). XRF analysis of rocks and minerals for major and trace elements on a single low dilution Li-tetraborate fused bead. *Advances in X-Ray Analysis*, *41*, 843–867.

Jung, H., Katayama, I., Jiang, Z., Hiraga, T., & Karato, S. (2006). Effect of water and stress on the lattice-preferred orientation of olivine. *Tectonophysics*, *421*, 1–22. https://doi.org/10.1016/j.tecto.2006.02.011

Karato, S., Toriumi, M., & Fujii, T. (1980). Dynamic recrystallization of olivine single crystals during high temperature creep. *Geophysical Research Letters*, *7*(9), 649–652.

Kassner, M. E., & Hayes, T. A. (2003). Creep cavitation in metals. *International Journal of Plasticity*, *19*(10), 1715–1748. https://doi.org/10.1016/S0749-6419(02)00111-0

Katayama, I., & Karato, S. (2008). Low-temperature, high-stress deformation of olivine under water-saturated conditions. *Physics of the Earth and Planetary Interiors*, *168*, 125–133. https://doi.org/10.1016/j.pepi.2008.05.019

Kuna, V. M., Nábělek, J. L., & Braunmiller, J. (2019). Mode of slip and crust-mantle interaction at oceanic transform faults. *Nature Geoscience*, *12*(February), 1. https://doi.org/10.1038/s41561-018-0287-1

Lafuente, B., Downs, R. T., Yang, H., & Stone, N. (2015). The power of databases: The RRUFF project. In *Highlights in Mineralogical Crystallography* (pp. 1–29). https://doi.org/10.1515/9783110417104-003

Lespinasse, M. (1999). Are fluid inclusion planes useful in structural geology? *Journal of Structural Geology*, *21*(8–9), 1237–1243. https://doi.org/10.1016/S0191-8141(99)00027-9

Lin, A., Tanaka, N., Uda, S., & Satish-Kumar, M. (2003). Repeated coseismic infiltration of meteoric and seawater into deep fault zones: A case study of the Nojima fault zone, Japan. *Chemical Geology*, *202*, 139–153. https://doi.org/10.1016/S0009-2541(03)00262-6

Linckens, J., Herwegh, M., Mntener, O., & Mercolli, I. (2011). Evolution of a polymineralic mantle shear zone and the role of second phases in the localization of deformation. *Journal of Geophysical Research - Solid Earth*, *116*(6), 1–21. https://doi.org/10.1029/2010JB008119

Maia, M., Sichel, S., Briais, A., Brunelli, D., Ligi, M., Ferreira, N., & Oliveira, P. (2016). Extreme mantle uplift and exhumation along a transpressive transform fault. *Nature Geoscience*, *9*(8), 619–623. https://doi.org/10.1038/ngeo2759

Matysiak, A. K., & Trepmann, C. A. (2012). Crystal-plastic deformation and recrystallization of peridotite controlled by the seismic cycle. *Tectonophysics*, *530–531*, 111–127. https://doi.org/10.1016/j.tecto.2011.11.029

McGuire, J. J., Collins, J. A., Gouédard, P., Roland, E., Lizarralde, D., Boettcher, M. S., & van der Hilst, R. D. (2012). Variations in earthquake rupture properties along the Gofar transform fault, East Pacific Rise. *Nature Geoscience*, *5*(5), 336–341. https://doi.org/10.1038/ngeo1454

McKenzie, D., Jackson, J., & Priestley, K. (2005). Thermal structure of oceanic and continental lithosphere. *Earth and Planetary Science Letters*, *233*, 337–349. https://doi.org/10.1016/j.epsl.2005.02.005

McNamara, D. D., Wheeler, J., Pearce, M., & Prior, D. J. (2012). Fabrics produced mimetically during static metamorphism in retrogressed eclogites from the Zermatt-Saas zone, Western Italian Alps. *Journal of Structural Geology*, *44*, 167–178. https://doi.org/10.1016/j.jsg.2012.08.006

Mei, S., Suzuki, A. M., Kohlstedt, D. L., Dixon, N. A., & Durham, W. B. (2010). Experimental constraints on the strength of the lithospheric mantle. *Journal of Geophysical Research - Solid Earth*, *115*(8), 1–9. https://doi.org/10.1029/2009JB006873

Mitchell, T. M., & Faulkner, D. R. (2009). The nature and origin of off-fault damage surrounding strike-slip fault zones with a wide range of displacements: A field study from the Atacama fault system, northern Chile. *Journal of Structural Geology*, *31*(8), 802–816. https://doi.org/10.1016/j.jsg.2009.05.002

Mitchell, Thomas M., Cembrano, Jose M., Fujita, K., Hoshino, K., Faulkner, D. R., Perez-Flores, P., Gomila, R. (2017). Fluid inclusion evidence of co-seismic fluid flow induced by dynamic rupture. In *Fault Zone Dynamic Processes: Evolution of Fault Properties During Seismic Rupture, AGU Monograph 227*, 37–45.

Montési, L. G. J., & Hirth, G. (2003). Grain size evolution and the rheology of ductile shear zones: From laboratory experiments to post-seismic creep. *Earth and Planetary Science Letters*, *211*, 97–110. https://doi.org/10.1016/S0012-821X(03)00196-1

Ohuchi, T., Kawazoe, T., Higo, Y., Funakoshi, K. -i., Suzuki, A., Kikegawa, T., & Irifune, T. (2015). Dislocation-accommodated grain boundary sliding as the major deformation mechanism of olivine in the Earth's upper mantle. *Science Advances*, 1–10. https://doi.org/10.1126/sciadv.1500360

Poirier, J. P. (1980). Shear localization and shear instability in materials in the ductile field. *Journal of Structural Geology*, *2*, 135–142. https://doi.org/10.1016/0191-8141(80)90043-7

Précigout, J., Prigent, C., Palasse, L., & Pochon, A. (2017). Water pumping in mantle shear zones. *Nature Communications*, *8*(15736), 1–10. https://doi.org/10.1038/ncomms15736

Précigout, J., & Stünitz, H. (2016). Evidence of phase nucleation during olivine diffusion creep: A new perspective for mantle strain localisation. *Earth and Planetary Science Letters*, *455*, 94–105. https://doi.org/10.1016/j.epsl.2016.09.029

Prigent, C., Guillot, S., Agard, P., & Ildefonse, B. (2018). Fluid-assisted deformation and strain localization in the cooling mantle wedge of a young subduction zone (Semail Ophiolite). *Journal of Geophysical Research: Solid Earth*, *123*, 7529–7549. https://doi.org/10.1029/2018JB015492

Putnis, A. D., Nidermeier, R. D., & Putnis, C. V. (2006). From epitaxy to topotaxy: The migration of reaction interfaces through crystals. *Geochimica et Cosmochimica Acta*, *70*(18), A509–A509. https://doi.org/10.1016/j.gca.2006.06.1479

Rice, J. R., Sammis, C. G., & Parsons, R. (2005). Off-fault secondary failure induced by a dynamic slip pulse. *Bulletin of the Seismological Society of America*, *95*(1), 109–134. https://doi.org/10.1785/0120030166

Roland, E., Lizarralde, D., McGuire, J. J., & Collins, J. A. (2012). Seismic velocity constraints on the material properties that control earthquake behavior at the Quebrada-Discovery-Gofar transform faults, East Pacific Rise. *Journal of Geophysical Research*, *117*, B11102. https://doi.org/10.1029/2012JB009422

Ryan, W. B. F., Carbotte, S. M., Coplan, J. O., O'Hara, S., Melkonian, A., Arko, R., & Zemsky, R. (2009). Global multi-resolution topography synthesis. *Geochemistry, Geophysics, Geosystems*, *10*, Q03014. https://doi.org/10.1029/2008GC002332

Sack, R. O., & Ghiorso, M. S. (1991). An internally consistent model for the thermodynamic properties of Fe-Mg-titanomagnetite-aluminate spinels. *Contributions to Mineralogy and Petrology*, *106*(4), 474–505.

Schmatz, J., & Urai, J. L. (2010). The interaction of fluid inclusions and migrating grain boundaries in a rock analogue: Deformation and annealing of polycrystalline camphor-ethanol mixtures. *Journal of Metamorphic Geology*, *28*(1), 1–18. https://doi.org/10.1111/j.1525-1314.2009.00849

Schmatz, J., & Urai, J. L. (2011). The interaction of migrating grain boundaries and fluid inclusions in naturally deformed quartz: A case study of a folded and partly recrystallized quartz vein from the Hunsrück Slate, Germany. *Journal of Structural Geology*, *33*(4), 468–480. https://doi.org/10.1016/j.jsg.2010.12.010

Sibson, R. H., Moore, J. M., & Rankin, A. H. (1975). Seismic pumping a hydrothermal fluid transport mechanism. *Journal of the Geological Society of London*, *131*, 653–659. https://doi.org/10.1016/j.nimb.2018.04.020

Skemer, P., Katayama, I., Jiang, Z., & Karato, S. (2005). The misorientation index: Development of a new method for calculating the strength of lattice-preferred orientation. *Tectonophysics*, *411*, 157–167. https://doi.org/10.1016/j.tecto.2005.08.023

Spruzeniece, L., & Piazolo, S. (2015). Strain localization in brittle-ductile shear zones: Fluid-abundant vs. fluid-limited conditions (an example from Wyangala area, Australia). *Solid Earth*, *6*(3), 881–901. https://doi.org/10.5194/se-6-881-2015

Tasaka, M., Hiraga, T., & Zimmerman, M. E. (2013). Influence of mineral fraction on the rheological properties of forsterite + enstatite during grain-size-sensitive creep: 2. Deformation experiments. *Journal of Geophysical Research: Solid Earth*, *118*, 3991–4012. https://doi.org/10.1002/jgrb.50284

Townend, J., & Zoback, M. D. (2000). How faulting keeps the crust strong. *Geology*, *28*(5), 399–402. https://doi.org/10.1130/0091-7613(2000)28<399:HFKTCS>2.0.CO;2

Tuttle, O. F. (1949). Structural petrology of planes of liquid inclusions. *The Journal of Geology*, *57*(4), 331–356. Retrieved from. http://www.jstor.org/stable/30056902

Van der Wal, D., Chopra, P., Drury, M., & Gerald, J. F. (1993). Relationships between dynamically recrystallized grain size and deformation conditions in experimentally deformed olivine rocks. *Geophysical Research Letters*, *20*(14), 1479–1482. https://doi.org/10.1029/93GL01382

van Roermund, H. L. M., & Boland, J. N. (1981). The dislocation substructures of naturally deformed omphacites. *Tectonophysics*, *78*, 403–418. https://doi.org/10.1016/0040-1951(81)90022-6

Wanamaker, B. J., & Evans, B. (1985). Experimental diffusional crack healing in olivine. *AGU Monograph*, *31*, 194–210.

Wanamaker, B. J., Wong, T.-F., & Evans, B. (1990). Decrepitation and crack healing of fluid inclusions in San Carlos olivine. *Journal of Geophysical Research*, *95*(B10), 15,623–15,641.

Warren, J. M., & Hirth, G. (2006). Grain size sensitive deformation mechanisms in naturally deformed peridotites. *Earth and Planetary Science Letters*, *248*, 438–450. https://doi.org/10.1016/j.epsl.2006.06.006

Warren, J. M., Shimizu, N., Sakaguchi, C., Dick, H. J. B., & Nakamura, E. (2009). An assessment of upper mantle heterogeneity based on abyssal peridotite isotopic compositions. *Journal of Geophysical Research*, *114*, B12203. https://doi.org/10.1029/2008JB006186

White, S. H., Burrows, S. E., Carreras, J., Shaw, N. D., & Humphreys, F. J. (1980). On mylonites in ductile shear zones. *Journal of Structural Geology*, *2*, 175–187. https://doi.org/10.1016/0191-8141(80)90048-6

Wolfson-Schwehr, M., & Boettcher, M. S. (2019). Global characteristics of oceanic transform fault structure and seismicity. In *Transform Plate Boundaries and Fracture Zones* (21–59). Elsevier Inc. https://doi.org/10.1016/B978-0-12-812064-4.00002-5

Wolfson-Schwehr, M., Boettcher, M. S., & Behn, M. D. (2017). Thermal segmentation of mid-ocean ridge-transform faults. *Geochemistry, Geophysics, Geosystems*, *18*, 1–14. https://doi.org/10.1002/2017GC006967

Wolfson-Schwehr, M., Boettcher, M. S., McGuire, J. J., & Collins, J. A. (2014). The relationship between seismicity and fault structure on the Discovery transform fault, East Pacific Rise. *Geochemistry, Geophysics, Geosystems*, *15*, 3698–3712. https://doi.org/10.1002/2014GC005445